Bursting of a laminar separation bubble subject to periodic forcing on a pitching airfoil

Connor Toppings, Theodoros Michelis, and Marios Kotsonis
Faculty of Aerospace Engineering, Delft University of Technology, Delft, South Holland, 2629 HS, Netherlands

Serhiy Yarusevych*
Department of Mechanical and Mechatronics Engineering, University of Waterloo, Waterloo, Ontario, Canada N2L 3G1

(Received 27 January 2026; accepted 15 June 2026; published 14 July 2026)

The bursting of a laminar separation bubble subject to periodic forcing is studied experimentally on a NACA0018 airfoil at a chord Reynolds number of 7×10^4. Bursting of the bubble is initiated by a dynamic ramp increase in angle of attack past the static stall angle with a nondimensional pitch rate of 0.008. The initial and final effective angles of attack are 4.9° and 7.2°. Periodic forcing is continuously applied to the boundary layer by a spanwise-uniform alternating current dielectric-barrier-discharge plasma actuator at the leading edge of the airfoil. The forcing frequency was chosen to match the unforced vortex shedding frequency of the separated shear layer at the initial angle of attack. Surface pressure and particle image velocimetry measurements were obtained during the airfoil motion to investigate the boundary layer development on the suction surface. In the unforced flow, bursting of the laminar separation bubble begins before the maximum angle of attack is reached. The results show that periodic forcing can either delay or prevent the onset of bursting past the end of the pitching motion. With increasing forcing amplitude, the laminar separation bubble may persist at the maximum angle of attack for on the order of 100 convective time units before bursting. Although periodic forcing can delay bursting, the dynamics of the bursting process are largely unchanged once the bursting process initiates, requiring a period of approximately 30 convective time units for the flow to settle to a massively separated state. The delay in the onset of bursting increases and becomes less deterministic as the forcing amplitude increases, until the forcing amplitude is sufficient to prevent bursting entirely.

DOI: 10.1103/zh15-87h3

I. INTRODUCTION

Lifting surfaces at aerodynamically low chord Reynolds numbers ($\mathrm{Re}_c < 5 \times 10^5$) typically experience abrupt stall when subject to an increase in angle of attack [1]. Many applications of lifting surfaces at low chord Reynolds numbers, including the wings of small unmanned air vehicles [2] and small wind turbines [3], operate in unsteady conditions where incoming velocity fluctuations

*Contact author: syarus@uwaterloo.ca

Published by the American Physical Society under the terms of the Creative Commons Attribution 4.0 International license. Further distribution of this work must maintain attribution to the author(s) and the published article's title, journal citation, and DOI.

cause rapid changes in the effective angle of attack. Thus, the unfavourable stalling characteristics experienced by these lifting surfaces may lead to severe unsteady loading [2].

At relatively low Reynolds numbers and freestream turbulence intensities, the boundary layers on a lifting surface often remain laminar into the region of adverse pressure gradient where they are susceptible to separation [4]. The inflectional instability, which becomes active in the region of adverse pressure gradient, becomes the dominant instability mechanism downstream of separation [5]. If the Reynolds number is sufficiently high, the convective amplification of disturbances in the separated laminar shear layer leads to transition through the quasiperiodic formation of spanwise roll-up vortices that undergo deformations and break down into three-dimensional turbulence, e.g., Ref. [6]. If the adverse pressure gradient is not too severe, the developing turbulent shear layer may reattach to the surface, enclosing in the time-average sense a thin region of recirculating flow known as a laminar separation bubble (LSB) [7]. In the upstream part of an LSB, the flow is nearly stagnant, producing a plateau in the lifting surface's pressure distribution, whereas in the downstream portion of the LSB there is relatively strong reverse flow and a more rapid pressure rise [7]. LSBs that are relatively small and do not substantially modify the pressure distribution compared to a hypothetical fully attached flow are termed "short" [4].

The abrupt stalling characteristics of low Reynolds number lifting surfaces are the result of a sudden failure of the reattachment process in a short LSB, known as bursting [8]. Bursting occurs when the rate of wall-normal momentum transfer across the transitioning shear layer is unable to overcome the adverse pressure gradient [8]. The rate of wall-normal momentum transfer is influenced by the characteristics of the roll-up vortices formed in the transition process, which depend on the spectrum of external disturbances and the stability properties of the attached laminar boundary layer and separated shear layer. For example, [9] and [10] reported that a reduction in initial disturbance amplitudes can lead to bursting, and [10] observed a reduction in the spanwise coherence of the roll-up vortices that occurred during bursting. Bursting leads either to the formation of a "long" LSB or to complete cessation of reattachment, both of which are associated with a substantial reduction in leading-edge suction [4].

Several recent investigations have considered the role of LSB bursting in the dynamic stall process, e.g., Refs. [11–14]. During an increase in angle of attack, the adverse pressure gradient on the suction surface is reduced relative to an equivalent static angle of attack [15]. As a consequence, the locations of laminar separation, transition, and reattachment on a dynamically pitching airfoil lag those on an airfoil undergoing a quasisteady change in angle of attack [11,16]. At higher Reynolds numbers ($\mathrm{Re}_c \sim 10^6$), a relatively small LSB may form near the leading edge that bursts when the progressive upstream movement of the turbulent separation location reaches the LSB [12]. At low chord Reynolds numbers, dynamic stall can be initiated by LSB bursting, leading to an abrupt separation of the reattaching turbulent boundary layer [11]. Alferez *et al.* [17] reported that the bursting process begins with a period of relatively slow increase in LSB length while LSB height remains largely unchanged, followed by a period of rapid expansion in LSB length and height. Kern *et al.* [14] associated the rapid expansion of the LSB during bursting with the formation of shear layer roll-up vortices of increased size and strength. The conditions under which LSB bursting occurs during dynamic motions are sensitive to external perturbations. Damiola *et al.* [13] found that elevated levels of freestream turbulence intensity delay stall during dynamic pitching motions.

One strategy for reducing the susceptibility of lifting surfaces to abrupt stall at low Reynolds numbers is through active control of the separating shear layer with the goal of maintaining reattachment in operating conditions that would otherwise lead to LSB bursting, e.g., Refs. [11,18–21]. During dynamic stall, such active control can delay LSB bursting and increase maximum suction [11,18,20]. By targeting the unstable frequency band of the separated shear layer with periodic forcing, a relatively large control effect can be realised for relatively little energy input [21]. The most substantial reduction in LSB size occurs when the forcing frequency matches the most amplified frequency in the separated laminar shear layer, typically on the order of $fc/u_\infty \sim 10$ for short LSBs, e.g., Refs. [22,23]. Forcing at this frequency causes a reduction in LSB length and height through earlier shear layer roll-up and reattachment [24,25]. Increasing the forcing amplitude

causes a larger reduction in LSB size [9,25]. Through its effect on the global pressure distribution, the decrease in LSB size leads to a delay in laminar separation [24]. Due to the substantial alteration in the mean flow field, the most amplified frequency of the forced LSB is greater than that of the unforced LSB [9]. Additionally, perturbation growth rates in the forced LSB are reduced due to the reduction in its thickness [9]. Periodic forcing at the most amplified frequency of the separated shear layer can also cause an LSB to form in conditions where the unforced flow experiences massive separation, e.g., Refs. [19,21]. The optimal forcing frequencies for reattachment on fully stalled airfoils are typically $fc/u_\infty \sim 1$ [19,26]. Periodic forcing at frequencies substantially lower or higher than the most amplified frequency are relatively ineffective for promoting transition and reattachment [11,21].

The introduction of periodic forcing affects the growth rates of secondary instabilities and the breakdown of the shear layer vortices into three-dimensional turbulence [11], which in turn affects the ability of the separated shear layer to reattach [21]. Although two-dimensional forcing causes earlier shear layer roll-up and increases the spanwise coherence of the shear layer vortices [11,27], the consequent delay in spanwise vortex deformations may lead to a delay in transition [11]. However, Ramos *et al.* [28] reported that two-dimensional forcing was more effective for increasing the lift-to-drag ratio during periodic plunging than three-dimensional forcing, attributing the greater effectiveness of two-dimensional forcing to the formation of a train of leading edge vortices rather than the single dynamic stall vortex formed with three-dimensional forcing or unforced conditions.

Prior studies have established that the LSB bursting process involves a substantial change in the band of unstable disturbances and the characteristics of vortical structures formed in the transition process when compared to short LSBs, e.g., Refs. [29,30]. However, it is unclear how the transient dynamics of the bursting process during a change in lifting surface operating conditions are affected by two-dimensional periodic forcing, which also modifies the stability and vortex shedding characteristics of LSBs [9,27]. Furthermore, it is inevitable that any device incorporating flow control will experience off-design operating conditions. Therefore, it is of interest to elucidate the flow development when a controlled LSB undergoes a transient change in operating conditions. The most critical change in operating conditions from a performance perspective is expected to be one from a condition where reattachment naturally occurs to one where reattachment does not naturally occur.

The objective of this study is to understand how two-dimensional periodic forcing affects the dynamics of the transition and reattachment processes in an LSB undergoing a change in global operating conditions. Specifically, this study is focused on a change in angle of attack. Toward this end, wind tunnel experiments were performed on a pitching airfoil model equipped with a spanwise uniform alternating current dielectric barrier discharge (AC-DBD) plasma actuator, e.g., Ref. [31] for periodic forcing of the boundary layer near the leading edge. Surface pressure and time-resolved particle image velocimetry (PIV) measurements were conducted to gain insight into the transient flow development over the suction surface of the airfoil.

II. EXPERIMENTAL METHODS

A. Model and facility

Wind tunnel tests on an aluminium NACA 0018 airfoil model were performed in the open jet A-tunnel at Delft University of Technology [32]. The jet nozzle was configured with a rectangular opening with dimensions 0.4 m × 0.7 m. The spatial uniformity of the core of the open jet is within 0.6% of the mean freestream velocity [32]. The airfoil model having a chord (c) of 0.2 m spanned the entire 0.4 m distance between the two side-walls attached to the jet nozzle opening. The ratio of the airfoil span to the maximum projected airfoil thickness in this experiment was 7.75. This is in line with the guidance from studies of two-dimensional airfoils [33] and bluff bodies [34] that recommend a minimum ratio of span to projected model thickness of approximately 7.5 to mitigate end-wall effects on the flow development at the midspan. The ends of the airfoil model were fixed

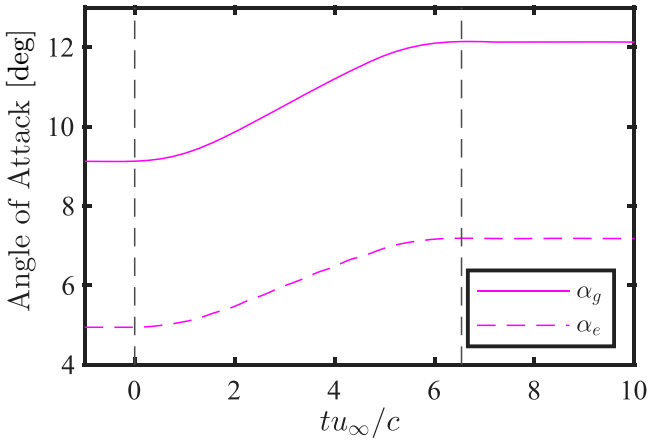


FIG. 1. Controlled transient changes in angle of attack. α_g: geometric angle of attack, α_e: effective angle of attack. Vertical dashed lines: start and end of pitching motion.

to two rotating circular acrylic end plates that provided optical access for PIV measurements. The spanwise uniformity of the flow over the midspan of the model in this setup was confirmed using a separate but geometrically identical NACA 0018 airfoil model with multiple rows of spanwise pressure taps. At comparable Reynolds numbers and angles of attack, the mean pressure coefficients on that model were within 6% of the spanwise mean. The present experiments were conducted at a chord Reynolds number (Re_c) of 7.0×10^4 corresponding to a freestream velocity (u_∞) of $5.46\,\mathrm{ms}^{-1}$. Under these conditions, the turbulence intensity measured at the center of the jet nozzle exit without the airfoil model or side-walls was measured to be less than 0.15% [32]. The presence of side-walls increases the turbulence intensity by approximately 0.1% [35], to an overall turbulence intensity of approximately 0.25% without the airfoil installed.

B. Transient pitching motions

To enable controlled pitching motions, the airfoil model was rotated about its quarter-chord location by a Zaber X-RSB120AB-E08 rotary stage. Transient ramp changes in angle of attack were performed from an initial geometric angle of attack (α_g) of 9° to a final geometric angle of attack of 12°. The initial and final angles were chosen to be equidistant from the geometric stall angle of $10.5° \pm 0.25°$ determined from surface pressure measurements in steady-state conditions. Thus, the corresponding limiting conditions represent an LSB state and a stalled state at the lower and higher angle of attack, respectively. The pitching motions were performed at a mean nondimensional pitch rate of $\dot{\alpha_g} c/(2u_\infty) = 0.008$. The equivalent reduced frequency for a periodic pitching motion with a period equal to twice that of the upward-only pitching motion is $f\pi c/u_\infty = 0.24$. The motion of the rotary stage during the transient pitching motions was measured with an Elap REV630 encoder with an angular resolution of 0.0025°. The geometric angle of attack was set using a negative of the airfoil profile with a flat back-side and a Wyler Clinotronic Plus digital protractor to align the chord of the airfoil to within 0.3°. The geometric angle of attack is plotted versus the nondimensional convective time (tu_∞/c) in Fig. 1.

Because the experiments were conducted in an open jet, deflection of the jet by the airfoil results in an effective angle of attack that is lower than the geometric angle of attack. It should be noted that a discrepancy between the geometric and effective angles of attack is unavoidable, even if a closed test section were used for the experiments, e.g., Ref. [36]. Since the purpose of this study is to understand the dynamics of LSB bursting in general, the precise values of the initial and final angles of attack are less important than the establishment of reattaching or separated flow

states at the initial and final conditions, respectively. Nonetheless, the effective angle of attack was estimated for completeness. To estimate the effective angle of attack accounting for the deflection of the open jet, universally accepted correction methods require the lift coefficient, e.g., Ref. [36]. In the present experiments, determination of the lift coefficient was complicated by the fact that pressure taps near the leading edge were covered by the dielectric material of the plasma actuator. Instead, the available surface pressure measurements away from the leading edge were used to identify a matching surface pressure distribution in a simulated unbounded flow using the XFOIL software [37]. Using surface pressure measurements from the initial angle of attack (LSB state), the angle of attack of the pressure distribution obtained from XFOIL that minimised the sum of squared errors with the measured pressure coefficients was taken to be the effective angle of attack. To obtain the effective angle of attack as a continuous function of geometric angle of attack, the following equation was used [35,36]:

$$\alpha_e = \alpha_g - AC_l(\alpha_e), \tag{1}$$

where A is a constant and C_l is the lift coefficient. With the effective angle of attack of the initial geometric angle of attack known from the comparison of surface pressure distributions, the constant A in Eq. (1) can be determined using the lift coefficient at the initial angle of attack computed using XFOIL. To determine the effective angles of attack throughout the pitching motion, Eq. (1) was iteratively solved using the previously determined value of A and the lift coefficient versus angle of attack relationship obtained from XFOIL computations. The initial and final limiting effective angles of attack estimated using this procedure were $\alpha_e = 4.9^\circ$ and 7.2°, respectively. The effective angle of attack throughout the transient pitching motion is plotted in Fig. 1. These effective angles of attack are approximately one-half of the geometric angle of attack, similar to the ratio of effective to geometric angle of attack of approximately one-half reported by Zang *et al.* (2022) for the same experimental setup. By comparing the effective angle of attack computed using Eq. (1) with A determined from measurements at $\alpha_g = 9^\circ$ to the surface pressure distribution from XFOIL with the closest agreement to surface pressure data obtained at $\alpha_g = 8^\circ$, the uncertainty in effective angle of attack was estimated to be 0.6°.

C. Measurement techniques

The freestream velocity at the outlet of the jet nozzle was measured using a pitot tube connected to a Honeywell HSC Series 025MD pressure transducer. An Omega PT100 RTD probe with an accuracy of 0.5% and an Amphenol NPA-201 barometric pressure sensor with an accuracy of 0.01% were used to measure the ambient temperature and pressure, respectively. Surface pressure measurements on the airfoil model were taken using a set of 22 pressure taps (10 on the suction surface and 13 on the pressure surface) connected to an array of Honeywell HSC series differential pressure transducers with a range of ± 160 Pa and an accuracy of ± 0.8 Pa. The pressure taps were staggered in the spanwise direction at an angle of 15° relative to the chord to mitigate interference effects between taps. The tubes connecting the surface pressure taps to the transducers had a length of 1 m and an inner diameter of 1 mm. Surface pressure measurements were obtained at a sampling frequency of 2 kHz during transient pitching motions and steady conditions at the initial and final angles of attack of the pitching motions. The pressure measurements in steady conditions were taken over a sampling period of $200c/u_\infty$, which is 3 orders of magnitude longer than the vortex shedding period of the LSB. For all steady-state mean pressure coefficients, the difference between those computed over $150c/u_\infty$ and $200c/u_\infty$ was less than 10%. The transient pressure measurements started $270c/u_\infty$ before the start of the pitch up motion and ended $400c/u_\infty$ after the end of the pitch up motion. The transient pressure measurements were taken over an ensemble of 20 runs of the pitching motion for each amplitude of periodic forcing.

Distortion caused by the tubing between the pressure taps and transducers was corrected using the Wiener deconvolution method described by Whitmore and Wilson [38]. The internal volume of the pressure transducers was neglected in this correction. The signal-to-noise ratio required

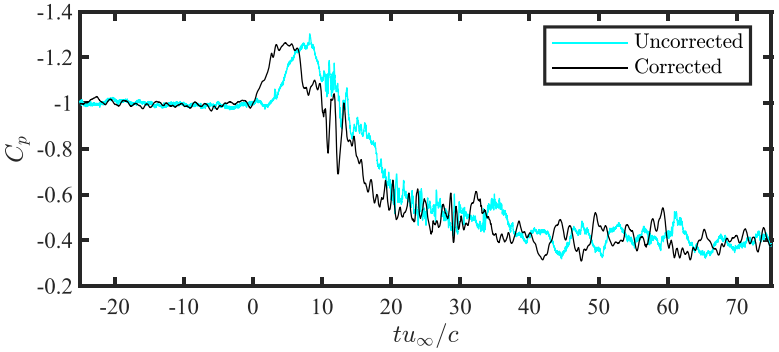


FIG. 2. Uncorrected and corrected pressure measurements from the pressure tap located at $x/c = 0.24$ on the suction surface during a transient pitch up motion without periodic forcing.

for the correction was estimated through the spectral fitting method [38] applied to data from pressure measurements in steady conditions under a laminar portion of the boundary layer. A comparison of the corrected and uncorrected pressure measurements from the pressure tap located at $x/c = 0.24$ on the suction surface during a transient pitch up motion without periodic forcing is presented in Fig. 2. The data is presented in terms of the pressure coefficient ($C_{\overline{p}} = 2(p - p_\infty)/(\rho u_\infty^2)$, where p is the surface pressure p_∞ is the free-stream pressure, and ρ is the air density). The most notable effect of the correction is to apply a phase shift to the pressure fluctuations.

PIV measurements were performed on the suction surface of the airfoil model during the controlled transient changes in angle of attack and in steady flow conditions corresponding to the initial and final angles of attack of the controlled pitching motions. The PIV measurements of the steady flow conditions at the final angle of attack were obtained $380c/u_\infty$ after the same pitching motion used for the transient PIV measurements. Particle images were acquired using a LaVision Imager Pro HS4 camera equipped with a Laowa 60 mm macro lens at an aperture of $f/4$. With the image sensor cropped to 1014×768 pixels, the field of view was approximately $0.65c \times 0.12c$ and the magnification factor was 0.16. Image pairs were recorded at a sampling frequency of 2 kHz. Illumination of the water-glycol fog particles introduced to the flow was provided by a Quantronix Darwin Duo Nd:YLF 527-80 M laser with a pulse separation of 80 µs. For each controlled change in angle of attack, a total of 5040 image pairs were recorded. Prior to vector calculation, all particle images were rotated so that the airfoil remained stationary in the field of view. Particle image preprocessing was performed using temporal sliding minimum subtraction with a window size of 9 images, spatial sliding minimum subtraction with a window size of 3 pixels, and local intensity normalisation with a window size of 7 pixels. Vector calculation was performed using the iterative multi-pass correlation method with window deformation implemented in the LaVision DaVis 10 software. The initial correlation window size was 32×32 pixels and the final correlation window size was 12×12 pixels with 75% overlap between windows, yielding a vector pitch of $0.001c$. The obtained velocity fields were transformed into the right-handed surface attached coordinate system defined in Fig. 3(a), where the origin is at the leading edge, the positive x and y axes are tangent and normal to the suction surface, respectively, and the z axis is in the spanwise direction. Using the correlation statistics method [39], the average uncertainty in instantaneous measurements of the u and v velocity components in the vicinity of the separated shear layer was estimated to be less than 10% of the freestream velocity. The relatively large uncertainty in the velocity measurements is partly due to the small correlation window employed for the purpose of increasing spatial resolution in the thin boundary layer near the separation point. The uncertainties in derived quantities were estimated using the methods described by Sciacchitano and Wieneke [40] and Moffat [41]. The uncertainty in the Reynolds shear stress in the vicinity of the separated shear layer for steady-state measurements was estimated to be less than $0.01u_\infty^2$. The corresponding uncertainty of the

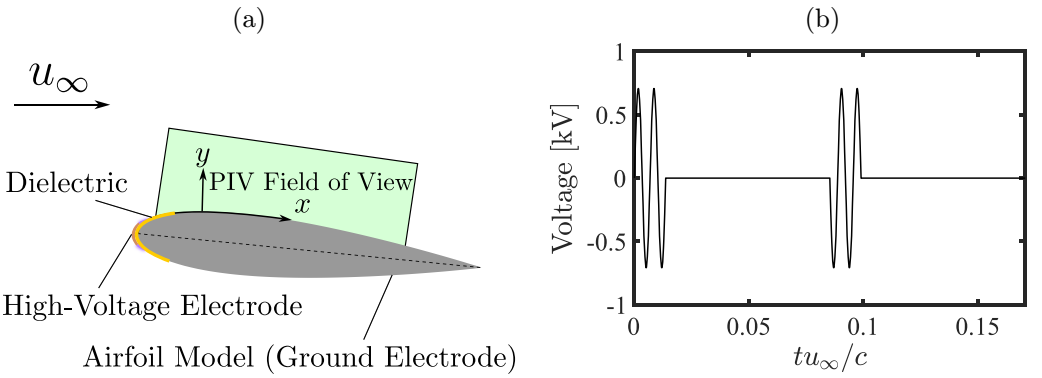


FIG. 3. Plasma actuator location (not to scale) and surface attached coordinate system definition (a), and plasma actuator voltage signal for $V_{pp} = 1.41$ kV (b).

temporally windowed Reynolds shear stress used to estimate the transition location in Sec. III C was estimated to be less than $0.013u_\infty^2$. PIV measurements of the transient flow development were taken over an ensemble of five runs of the pitching motion for each amplitude of periodic forcing.

For improved resolution of the boundary layer near the location of laminar separation, the average correlation method of Meinhart *et al.* [42] was employed for particle image processing. The average correlation method involves averaging the cross-correlation functions from multiple image pairs before computing the displacement of the cross-correlation peak. For the limiting flow states, the average correlation was computed over the complete set of acquired images for a given operating condition. For the transient pitching motions, the average correlation was computed over a sliding temporal kernel of seven image pairs. The final correlation window size for the average correlation method was 4×4 pixels ($3 \times 10^{-4}c$).

D. Periodic forcing

Periodic forcing of the attached boundary layer upstream of the LSB on the airfoil was performed using a spanwise-uniform AC-DBD plasma actuator at the leading edge of the airfoil. The high-voltage electrode, made from adhesive copper tape of width 12 mm and thickness 30 μm, was separated from the aluminium airfoil model by a layer of adhesive polyimide (Kapton) dielectric of width 50.8 mm and thickness 69 μm. The high-voltage electrode was centered at the leading edge, and the conductive aluminium airfoil model served as the ground electrode, making the locations of plasma discharge symmetric on the pressure and suction surfaces. The pressure side discharge is likely inconsequential for the boundary layer transition dynamics on the suction surface. The dielectric layer extended to $x/c = 0.08$ on the pressure surface and $x/c = 0.2$ on the suction surface, which was downstream of the laminar separation location to avoid tripping the suction surface boundary layer. A Trek 20/20C HS high-voltage amplifier was used to power the actuator. The applied voltage signal was a 4 kHz sine wave. This frequency was selected because plasma actuators typically require AC frequencies on the order of kilohertz to produce stable and uniform plasma discharges, e.g., Ref. [43]. This frequency is an order of magnitude greater than the hydrodynamic frequencies relevant to boundary layer transition on the suction surface. A preliminary spectral analysis of velocity fluctuations in the separated shear layer indicated that the vortex shedding frequency at the initial angle of attack of $\alpha_e = 4.9^\circ$ was approximately 320 Hz. To introduce disturbances to the boundary layer at this frequency, the sine wave voltage signal was modulated by a square wave with a frequency of 320 Hz. A relatively small 16% duty cycle was chosen for the square wave to reduce the strength of the forcing so that massive separation

occurred for low forcing amplitudes, and to produce an integer number of periods of the 4kHz signal in each pulse. An example of two periods of the modulated plasma actuator voltage signal is plotted in Fig. 3(b). The experiments of Yarusevych and Kotsonis [9] pertaining to LSBs forced by a plasma actuator in a similar manner at various modulation frequencies suggest that a deviation of the modulation frequency away from that of the vortex shedding frequency would reduce the effectiveness of the periodic forcing for maintaining reattachment.

Transient surface pressure and PIV measurements were performed for three levels of peak-to-peak voltage (V_{pp}). The forcing levels were selected to compare the unforced flow ($V_{pp} = 0\,\text{kV}$) to forcing that caused a measurable reduction in LSB size without suppressing LSB bursting during transient pitching motions ($V_{pp} = 0.78\,\text{kV}$ and $V_{pp} = 0.92\,\text{kV}$), and forcing at a level sufficient to suppress LSB bursting entirely ($V_{pp} = 1.41\,\text{kV}$). The maximum mean velocity magnitude induced by the plasma actuator at the highest forcing amplitude with 100% duty cycle in quiescent conditions was measured using PIV to be less than $0.01u_\infty$. In this study, the flow control strategy is to prevent stall by manipulating the amplitudes of amplified disturbances that lead to transition rather than by the direct addition of momentum to the boundary layer. Thus, the amplitude of velocity fluctuations at the forcing frequency in the separated shear layer is employed to quantify the effect of the plasma actuator in Sec. III.

E. Data processing methods

1. Transition location definition

Although the transition of the separated shear layer from laminar to turbulent states occurs over a finite streamwise distance, it is useful to define a transition point so that changes in the transition location can be quantified [44]. The transition criterion used in the present work is the same as the one used by Ol *et al.* [45] and Hain *et al.* [46], except that the boundary layer edge velocity is used in the present work instead of the free-stream velocity. Specifically, the transition point (x_t) is defined as the x location where the Reynolds shear stress ($-\overline{u'v'}$) measured at the y coordinate equal to the displacement thickness first exceeds $0.001u_e^2$, where u_e is the maximum streamwise velocity measured at a given x location. The displacement thickness is defined as $\delta^* = \int_0^\delta (1 - u/u_e)dy$, where δ is the boundary layer thickness (i.e., the y location where u_e occurs). This transition criterion is employed because it is applicable to both reattaching and massively separated flows.

2. Time-frequency analysis

A time-frequency analysis of wall-normal velocity fluctuations (v') near the transition location during transient pitching motions was performed using the continuous wavelet transform. The continuous wavelet transform (Ψ) with respect to the wavelet ψ is defined as [47]

$$\Psi(t, s) = \int_{-\infty}^{\infty} \frac{1}{s} \psi^* \left(\frac{\tau - t}{s} \right) v'(\tau) d\tau, \tag{2}$$

where t is time, s is the wavelet scale, and $*$ is the complex conjugate. An Airy wavelet with a duration of $\sqrt{120}$ was employed [47], for which the relationship between the wavelet scale and peak frequency are given by Lilly [48]. The wavelet transform was performed on the wall-normal fluctuating velocity component at the location $y = \delta^*$ over the streamwise range $x_t \leqslant c \leqslant x_t + 0.05c$, where there is a rapid increase in the magnitude of the Reynolds shear stress. The wavelet amplitude scalograms presented in Sec. III B were obtained after averaging the absolute value of the wavelet coefficients over $x_t \leqslant c \leqslant x_t + 0.05c$, and over the ensemble of PIV measurement runs.

TABLE I. Limiting LSB parameters and their uncertainties at $\alpha_e = 4.9^\circ$. Uncertainty intervals are at 95% confidence.

V_{pp}	x_s/c	x_t/c	x_r/c	h/c	h/h_0
0 kV	0.15 ± 0.02	0.39 ± 0.02	0.57 ± 0.02	0.029 ± 0.001	1
0.78 kV	0.15 ± 0.02	0.39 ± 0.02	0.54 ± 0.02	0.026 ± 0.001	0.89 ± 0.04
0.92 kV	0.15 ± 0.02	0.37 ± 0.02	0.52 ± 0.02	0.020 ± 0.001	0.70 ± 0.04
1.41 kV	0.19 ± 0.02	0.35 ± 0.02	0.43 ± 0.02	0.010 ± 0.001	0.36 ± 0.04

III. RESULTS AND DISCUSSION

A. Limiting flow states

The flow development on the suction surface of the airfoil in steady operating conditions at the initial angle of attack of $\alpha_e = 4.9^\circ$ is illustrated in Fig. 4, where mean streamwise velocity and Reynolds shear stress fields are presented for each amplitude of forcing. The mean streamwise velocity fields were obtained from the average correlation method, whereas the Reynolds shear stress fields were computed using the standard PIV method. The mean surface pressure coefficients ($C_{\overline{p}}$), and their standard deviations (σ_{C_p}) are plotted in Figs. 4(i) and 4(j), respectively. The locations of separation and reattachment were estimated from the dividing streamline, which was computed from the locus of points below which there is zero-net-streamwise mass flux. Because of the sensitivity of separation point estimates to PIV errors in the relatively thin shear layer near the separation location, a linear fit to the portion of the dividing streamline upstream of the location of maximum dividing streamline height was used to determine the location of separation, e.g., Ref. [49]. The location of transition was identified using the method described in Sec. II E 1. A summary of the LSB structure at the initial angle of attack for each forcing amplitude is provided in Table I. The table provides the locations of separation (x_s), transition (x_t), reattachment (x_r) and their respective uncertainty intervals (95% confidence). The maximum wall-normal distance of the dividing streamline (h) and its ratio to the maximum dividing streamline height in the unforced flow (h_0) is also tabulated. The relatively large uncertainty in x_s for $V_{pp} = 1.41$ kV is a consequence of the shallower angle of the dividing streamline for this forcing amplitude. Since x_s was estimated from the intersection of the dividing streamline with the model surface, a relatively small uncertainty in the angle of the dividing streamline leads to a larger uncertainty in the location of x_s when the angle between the dividing streamline and the surface reduces.

In the unforced flow at the initial angle of attack, there is a rapid increase in the magnitude of the Reynolds shear stress downstream of transition, and the highest magnitude of the Reynolds shear stress occurs near reattachment. As is typical for LSBs, the suction surface pressure distribution exhibits nearly constant pressure upstream of the location of maximum dividing streamline height [50] [Fig. 4(i)]. Downstream of the location of maximum bubble height, there is a relatively rapid increase in the mean and standard deviation of the surface pressure coefficient, consistent with those expected for transition and reattachment of the separated shear layer [7,51].

Plasma with $V_{pp} = 0.78$ kV [Fig. 4(c)] leads to a mild upstream movement of reattachment, e.g., Ref. [9]. For $V_{pp} = 0.92$ kV [Fig. 4(e)], there is a more substantial advancement of the reattachment location. For the highest forcing amplitude of $V_{pp} = 1.41$ kV [Fig. 4(g)], the height of the LSB is substantially reduced by $0.019c$ relative to the case of unforced flow. The corresponding surface pressure measurements display a notable upstream shift in the locations of pressure recovery and maximum pressure coefficient fluctuations, indicating a significant advancement of transition and reattachment. The relatively large decrease in bubble thickness at the highest forcing amplitude leads to a reduction in the magnitude of the peak Reynolds shear stress occurring near reattachment. This decrease is attributed to stabilisation of the separated shear layer due to its closer proximity to the wall [9,52]. The observed changes in LSB structure and transition dynamics caused by the

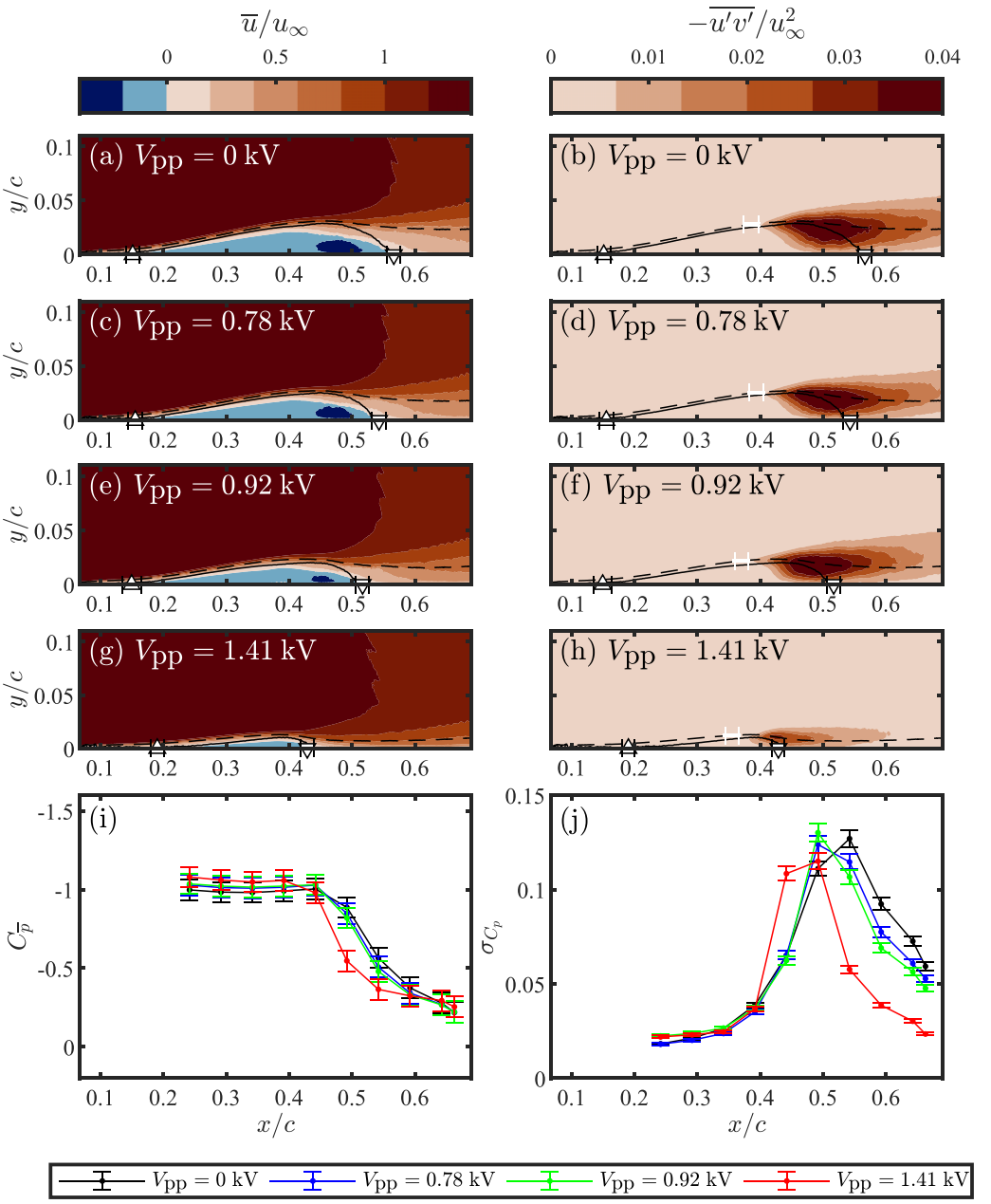


FIG. 4. Mean streamwise velocity (a), (c), (e), (g), mean surface pressure coefficient (i), Reynolds shear stress (b), (d), (f), (h), and standard deviation of suction surface pressure coefficient (g), in steady state at $\alpha_e = 4.9°$. Dashed lines: δ^*, solid lines: dividing streamline, $\triangle$: separation location, $\triangledown$: reattachment location, white markers: transition location.

periodic forcing are expected to influence the unsteady dynamics of the LSB bursting process when the operating conditions of the airfoil are changed. These unsteady dynamics will be explored in Sec. III B.

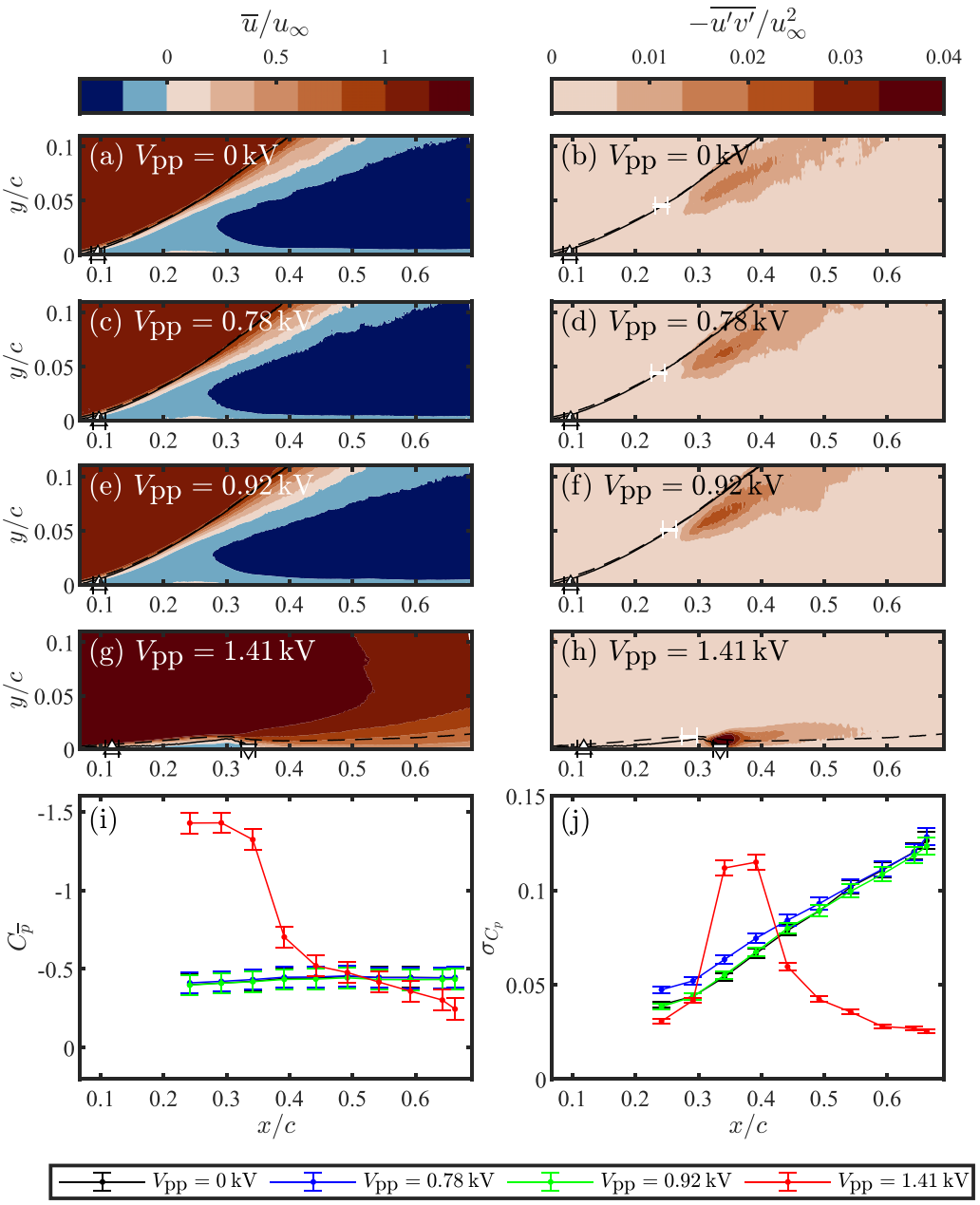


FIG. 5. Mean streamwise velocity (a), (c), (e), (g), mean surface pressure coefficient (i), Reynolds shear stress (b), (d), (f), (h), and standard deviation of suction surface pressure coefficient (g), in steady state at $\alpha_e = 7.2°$. Dashed lines: δ^*, solid lines: dividing streamline, $\triangle$: separation location, $\triangledown$: reattachment location, white markers: transition.

Mean streamwise velocity and Reynolds shear stress fields on the suction surface of the airfoil in steady operating conditions at the final angle of attack of $\alpha_e = 7.2°$ are presented in Fig. 5 for each forcing amplitude. The locations of separation, transition, reattachment, and maximum LSB height for each forcing amplitude at the final angle of attack are tabulated in Table II

TABLE II. Limiting separated flow and LSB parameters at $\alpha_e = 7.2^\circ$. Uncertainty intervals are at 95% confidence.

V_{pp}	x_s/c	x_t/c	x_r/c	h/c	h/h_0
0 kV	0.10 ± 0.02	0.24 ± 0.02			
0.78 kV	0.10 ± 0.02	0.24 ± 0.02			
0.92 kV	0.10 ± 0.02	0.25 ± 0.02			
1.41 kV	0.12 ± 0.02	0.28 ± 0.02	0.33 ± 0.02	0.010 ± 0.001	0.36 ± 0.04

with their corresponding uncertainty intervals (95% confidence). The increase in adverse pressure gradient with angle of attack leads to massive separation for the unforced flow and the two lowest amplitudes of periodic forcing, with nearly constant mean surface pressure in the separated flow region [Fig. 5(i)]. The stronger adverse pressure gradient at the final angle of attack also leads to an advancement of the transition location relative to the cases at the initial angle of attack.

There are no significant differences in the mean flow fields at the final angle of attack for $V_{pp} = 0$ kV to 0.92 kV [Figs. 5(a)–5(f)]. The similarity of the final flow states for all of the stalled conditions suggests that once the LSB bursts, a substantial change in the band of unstable frequencies occurs in the separated shear layer, which substantially reduces the effectiveness of the periodic forcing. Specifically, the decrease in the outer flow velocity in the stalled condition is expected to reduce the frequency of the most unstable disturbance well below that of the constant frequency of the periodic forcing [53]. However, increasing the forcing amplitude to $V_{pp} = 1.41$ kV [Figs. 5(g)–5(h)] is sufficient to enable the LSB to persist at $\alpha_e = 7.2^\circ$. At this forcing amplitude, reattachment is facilitated by a notably more rapid increase in Reynolds shear stress downstream of the transition location relative to that observed in the separated shear layer for lower forcing amplitudes. The upstream movement of the LSB at the final angle of attack relative to the initial angle of attack for the highest forcing amplitude is consistent with expected relationship between LSB location and angle of attack [53]. In agreement with the LSB location measured using PIV, the pressure distribution for $V_{pp} = 1.41$ at the final angle of attack displays a pressure recovery over the region $0.35 < x/c < 0.45$ and increased pressure coefficient fluctuations near the reattachment location.

The effect of the forcing amplitude on the convective growth of disturbances that lead to transition and the possibility of subsequent reattachment was quantified through spectral analysis of velocity fluctuations extracted from the separated shear layer at $y = \delta^*$. The wall-normal velocity fluctuations were used for the analysis because they are more strongly correlated to the passage of shear layer roll-up vortices than the streamwise velocity fluctuations, which are affected by low-frequency shear layer flapping to a greater extent [46,54]. Power spectra were computed from the extracted signals using Welch's method [55] with a window length of $7c/u_\infty$ and 50% overlap. The resulting frequency resolution is $0.14c/u_\infty$. The power spectral density (PSD) of the wall-normal fluctuating velocity signal ($\mathcal{P}_{v'v'}$) at the x location where the forcing frequency ($fc/u_\infty = 11.7$) attains its highest amplitude is presented in Figs. 6(a) to 6(b) for each forcing amplitude. The x locations of the spectra in Figs. 6(a) and 6(b) are indicated by the dashed lines in Figs. 6(c) and 6(d) which track the streamwise growth of the PSD at the forcing frequency.

The forcing frequency of $fc/u_\infty = 11.7$, which was chosen to target the band of unstable frequencies in the unforced flow, is the dominant peak in the spectra of the cases with forcing. As the amplitude of forcing is increased, the spectral power becomes less broadband and more concentrated at the forcing frequency. The two highest forcing levels exhibit notably increased spectral power density at the first sub-harmonic of the forcing frequency, suggesting that vortex merging may be more prevalent for these cases, e.g., Ref. [56]. For the unforced flow at $\alpha_e = 7.2^\circ$ [Fig. 6(b)] the spectral peak at a frequency of $fc/u_\infty \approx 4.3$ is consistent with the reduction in the most amplified frequency expected to occur as a result of massive separation, e.g., Ref. [53]. Since the

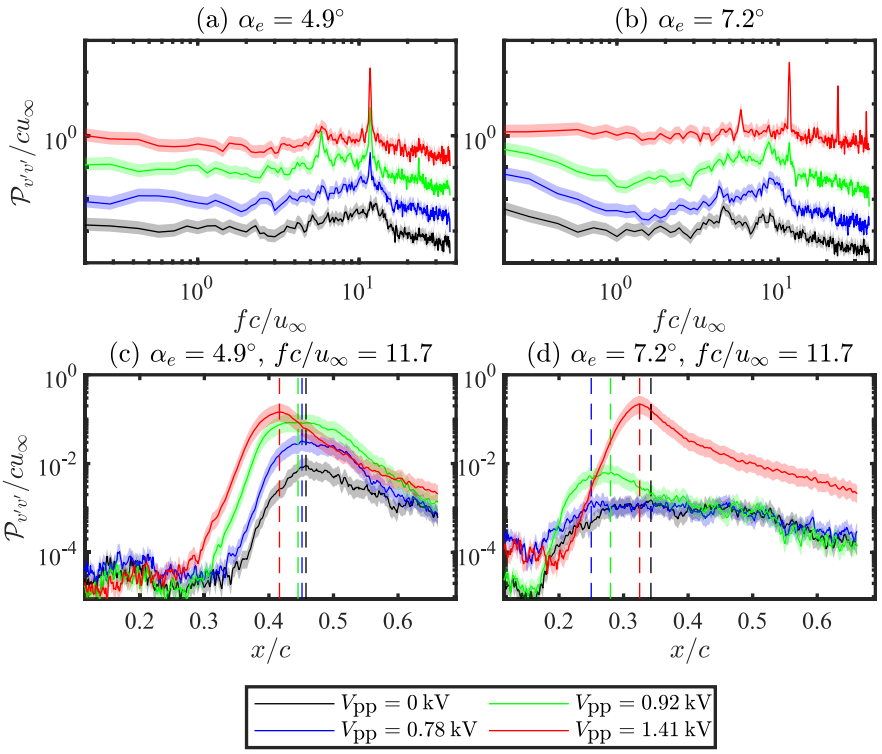


FIG. 6. Wall-normal fluctuating velocity spectra for initial (a) and final (b) flow states. Streamwise amplification of wall-normal velocity fluctuations at the frequency of periodic forcing for initial (c) and final (d) flow states. Each forcing amplitude in panels (a), (b) is shifted by an order of magnitude for clarity. Dashed lines in panels (c), (d) indicate location of spectra presented in panels (a), (b).

most amplified frequency in the massively separated flow is substantially lower than the forcing frequency, the forcing frequency is not significantly amplified for $V_{pp} = 0.78$ kV and 0.92 kV. Instead, the first harmonic of the unforced vortex shedding frequency ($fc/u_\infty = 8.7$) becomes the most amplified frequency for the lowest two amplitudes of forcing. The relatively strong amplification of the forcing frequency at the highest forcing amplitude for $\alpha_e = 7.2°$ is attributed to the strong interdependency of the mean flow and disturbance amplification, termed mean-flow-deformation [57]. It is likely that for the highest amplitude of periodic forcing, the mean-flow-deformation maintains the most amplified frequency relatively close to the forcing frequency. This is because the higher boundary layer edge velocity associated with the reduction in LSB size leads to an increase in the frequencies of unstable disturbances, e.g., Ref. [9]. Thus, the mean-flow-deformation may act as part of a positive feedback mechanism that locks the most amplified frequency to the frequency of the applied forcing when the forcing amplitude is sufficiently high, e.g., Ref. [58].

The PSD of the wall-normal fluctuating velocity signal at the forcing frequency ($fc/u_\infty = 11.7$) is plotted versus streamwise location in Figs. 6(c) and 6(d) for the initial and final limiting flow states, respectively, for each forcing amplitude. Applying periodic forcing at $V_{pp} = 0.78$ kV, 0.92 kV, and 1.41 kV increases the maximum $\mathcal{P}_{v'v'}$ of the forcing frequency at the initial angle of attack by approximately 4, 10, and 16 times relative to the unforced flow, respectively [Fig. 6(a)]. For the lowest two levels of forcing, the streamwise location of maximum $\mathcal{P}_{v'v'}$ at the forcing frequency is not significantly affected by the periodic forcing [Fig. 6(c)]. However, at $V_{pp} = 1.41$ kV, there is a more substantial upstream shift in the location of the maximum of $\mathcal{P}_{v'v'}$ to $x/c = 0.43$, consistent with the earlier transition to turbulence suggested by the mean velocity field and pressure

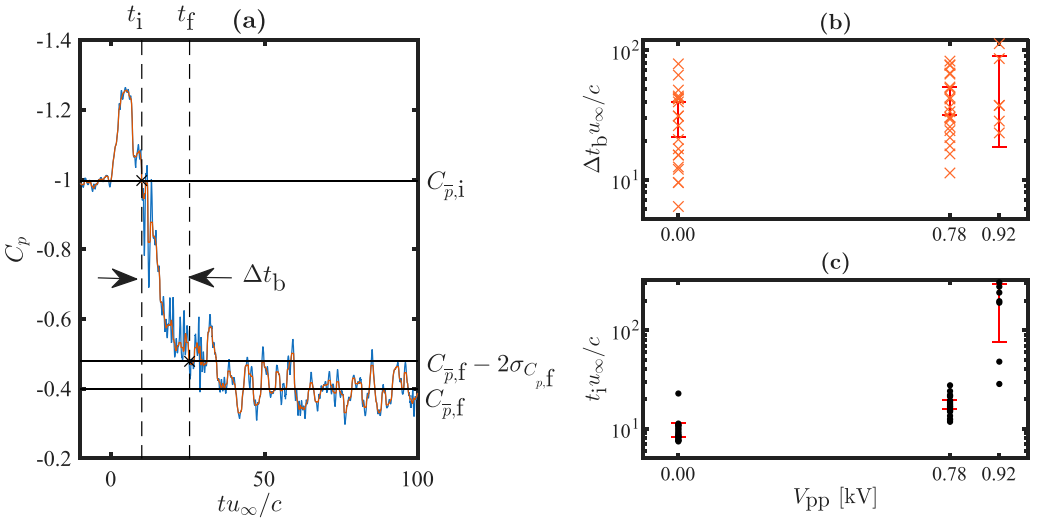


FIG. 7. Definition of bursting start time (t_i) and bursting duration (Δt_b) (a), bursting start times (b), and bursting durations (c). Blue line in panel (a): filtered pressure data; orange line in panel (a): moving median of filtered pressure data.

measurements for this case (Fig. 4). At $\alpha_\mathrm{e} = 7.2^\circ$ [Fig. 6(d)] for the cases where reattachment does not occur ($V_\mathrm{pp} = 0\,\mathrm{kV}$, $0.78\,\mathrm{kV}$, $0.92\,\mathrm{kV}$), there is significantly lower amplification of the forcing frequency. The relatively low amplitudes of velocity fluctuations at the forcing frequency in these cases is attributed to the change in stability characteristics of the massively separated flow relative to the reattaching flow. However, when the forcing amplitude is strong enough to maintain reattachment, the amplitude of velocity fluctuations at the forcing frequency saturates at a similar order of magnitude in both the initial and final limiting flow states.

B. Timescales of the transient bursting process

To quantify the time duration of the LSB bursting transient, the bursting transient duration (Δt_b) was computed from the surface pressure coefficient measured at $x/c = 0.24$ using the procedure illustrated in Fig. 7(a). The location of the pressure data used for this procedure was chosen within the dead-air region of the LSB [7] to reduce the influence of turbulent pressure fluctuations on the results. The start of the bursting transient (t_i) was defined as the last time that the pressure coefficient at $x/c = 0.24$ was less than its mean value in the initial flow state ($C_{\overline{p},\mathrm{i}}$), and the end of the bursting transient (t_f) was defined as the time that the pressure coefficient first exceeded the mean value of the final flow state ($C_{\overline{p},\mathrm{f}}$) minus two standard deviations of the pressure coefficient of the final flow state ($\sigma_{C_{p,\mathrm{f}}}$). The bursting transient duration was then defined as $\Delta t_\mathrm{b} = t_\mathrm{f} - t_\mathrm{i}$. To mitigate the influence of outliers, the foregoing procedure was performed on the moving median of the pressure coefficient computed over a temporal window of $2c/u_\infty$ [orange line in Fig. 7(a)]. Varying the length of the temporal window between c/u_∞ and $4c/u_\infty$ did not change the trends of the mean values of t_i and Δt_b with respect to forcing amplitude.

The bursting start times and bursting durations obtained from the 20 trials at all forcing levels are plotted in Figs. 7(b) and 7(c), respectively. The numbers of LSB bursting transients observed within the pressure measurement period of $400c/u_\infty$ after the beginning of the increase in angle of attack were 20, 20, 6, and 0 for forcing at $V_\mathrm{pp} = 0\,\mathrm{kV}$, $0.78\,\mathrm{kV}$, $0.92\,\mathrm{kV}$, and $1.41\,\mathrm{kV}$, respectively. The differences in mean bursting durations between forcing amplitudes are not statistically significant at a 95% confidence level [Fig. 7(d)]. These bursting durations are largely on the order of $10c/u_\infty$, similar to the durations of the bursting transients for LSBs in unforced conditions observed in

previous studies [30,59], and for bursting occurring after the cessation of forcing [20]. However, the uncertainty in the mean bursting duration is relatively large for the higher forcing amplitudes due to the smaller sample size of bursting events. The differences in mean bursting start time between each forcing level are statistically significant at a 95% confidence level [Fig. 7(c)], exhibiting an increase in the bursting start time with increasing forcing amplitude. Due to the increase in bursting start time with forcing amplitude, only 6 bursting events were observed within the measurement period for the second highest forcing amplitude. The increase in bursting start times with increasing forcing amplitude suggests that periodic forcing reduces the probability of LSB bursting per unit time while having a relatively weaker effect on the dynamics of the bursting process when it occurs.

The time-history of the surface pressure coefficients at $x/c = 0.24$ on the suction surface of the airfoil are plotted in Fig. 8 for all 20 runs at each forcing amplitude. In Figs. 8(a), 8(c), 8(e), and 8(g), the pressure coefficients are plotted versus the number of convective time units from the start of the pitching motion (tu_∞/c). The ensemble size of 20 runs was sufficient to ensure convergence of ensemble mean surface pressures within the instrument accuracy at forcing amplitudes for which LSB bursting was consistently triggered by the pitching motion. For the case of $V_{pp} = 0.92\,\text{kV}$, the flow itself does not converge to a single state after the pitching motion, rendering the convergence of the ensemble mean less meaningful. However, convergence of the multimodal probability density function of the transient pressure coefficients at $x/c = 0.24$ for $V_{pp} = 0.92\,\text{kV}$ was also confirmed for the ensemble of 20 runs. The pitch up motion causes an initial increase in suction to begin at $tu_\infty/c = 0$. In the unforced flow and for the lowest forcing amplitude [Figs. 8(a) and 8(c)], there is an overshoot in suction at the end of the pitch up motion before a more gradual decrease in suction associated with bursting of the LSB [4]. The overshoot is characteristic of the dynamic stall process, in which a transient increase in lift occurs beyond that attainable in steady conditions [60]. The overshoot occurs because of the relatively long time required for the flow to evolve from attached to stalled states compared to the period of the pitching motion, e.g., Ref. [61]. At the second highest forcing level [Fig. 8(e), $V_{pp} = 0.92\,\text{kV}$], increased suction persists after the pitching motion because the flow initially remains attached. However, this level of suction is unsustainable and bursting occurs at widely varying times for different runs. Thus, an increase in forcing amplitude enables the suction associated with the dead-air region of the LSB to be maintained for a longer period of time after the change in angle of attack. At the highest amplitude of forcing [Fig. 8(g), $V_{pp} = 1.41\,\text{kV}$], increased suction is maintained indefinitely after the increase in angle of attack and LSB bursting was never observed.

In Figs. 8(b), 8(d), and 8(f), the surface pressure coefficients at $x/c = 0.24$ have been shifted by the bursting start time t_i so that the loss of suction associated with LSB bursting begins at $t - t_i = 0$ for all runs at $V_{pp} = 0\,\text{kV}$, $0.78\,\text{kV}$, and $0.92\,\text{kV}$, respectively. Note, such a plot for $V_{pp} = 1.41\,\text{kV}$ is not presented since the LSB does not burst for $V_{pp} = 1.41\,\text{kV}$. The relatively large deviations of the individual runs from the ensemble-averages (black lines) for $t - t_i > 0$ highlight the significant run-to-run variability in the LSB bursting process. At higher forcing amplitudes, a greater degree of variability in the time-history of the pressure coefficients is observed. However, due to this variability and the relatively small ensemble size (20 runs), the differences between the computed ensemble-averaged surface pressure coefficients in Figs. 8(b), 8(d), and 8(f) are not statistically significant.

A comparison of instantaneous pressure distributions across the 10 pressure taps on the suction surface is facilitated by Fig. 9, which presents measurements from five trials for each forcing amplitude. The bursting start time (t_i) is indicated by the dashed lines in each plot. The pitch up motion, which is completed in 6 convective time units, initially causes an increase in suction in the LSB for $x/c \leqslant 0.5$. In the unforced flow [Fig. 9(a)], relatively large pressure fluctuations indicative of LSB bursting consistently begin to occur across the streamwise extent of the pressure measurements within $5c/u_\infty$ of the pitch up motion [cf. Fig. 8(a)]. The duration of these large pressure fluctuations varies substantially, with the leftmost run shown in Fig. 9(a) settling more quickly than the others. For $V_{pp} = 0.78\,\text{kV}$ [Fig. 9(b)], increased suction is maintained within

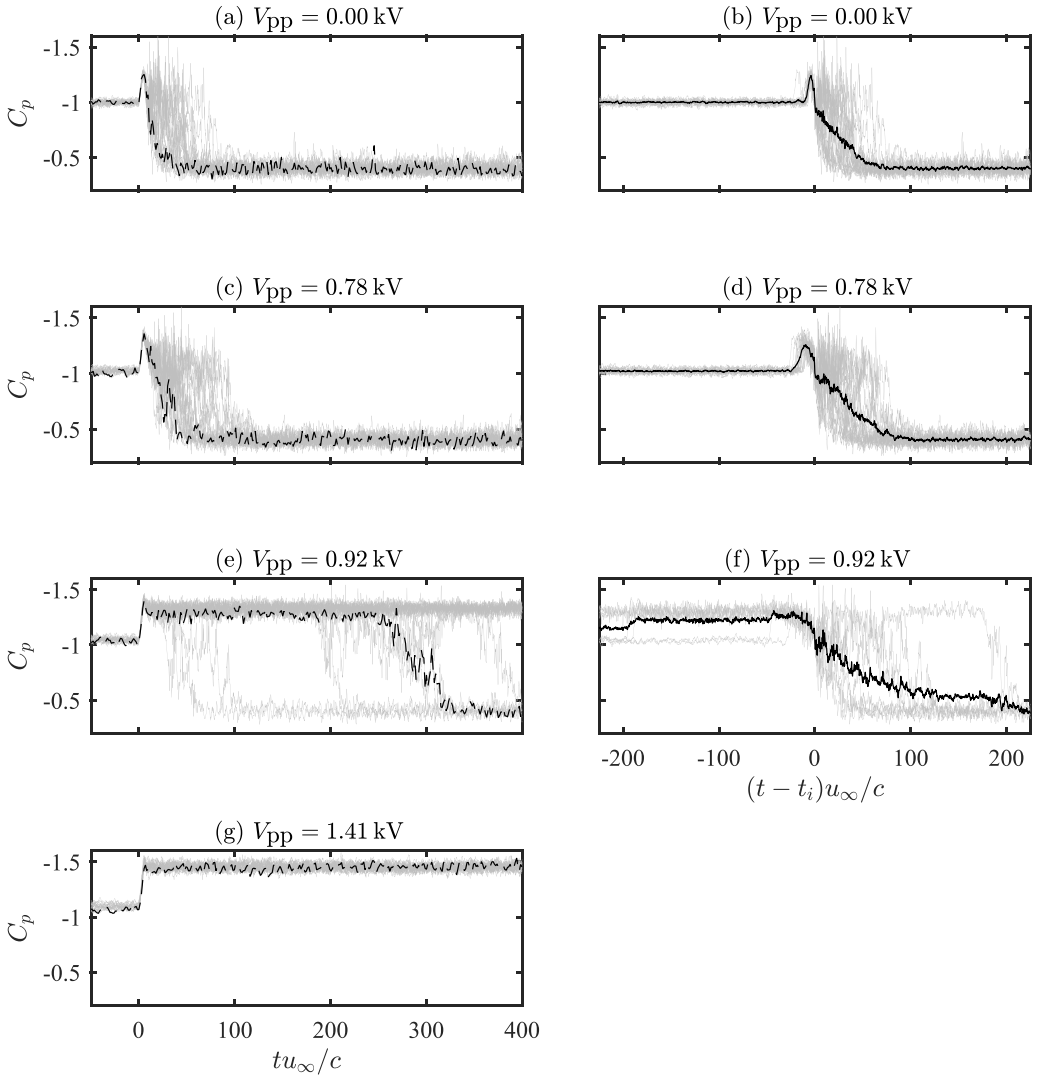


FIG. 8. Transient surface pressure coefficients at $x/c = 0.24$ for 20 runs aligned by pitching motion start time (a), (c), (e), (g) and bursting start time (b), (d), (e). Dashed lines in panels (a), (c), (e), (g) shown an example of a single run, solid lines in panels (b), (d), (e) are ensemble averages.

the LSB for a relatively longer period of time compared to the unforced flow before the large pressure oscillations begin. For $V_{\mathrm{pp}} = 0.92\,\mathrm{kV}$, there are large variations in the transient development of the pressure distribution between runs because the bursting start time varies widely. For three of the runs presented, increased suction is maintained such that LSB bursting does not occur until $tu_\infty/c > 100$. The substantial duration of time over which increased suction is maintained for $x/c < 0.4$ for some runs at this forcing amplitude indicates that an unsustainable LSB persists after the end of the increase in angle of attack. This suggests that $V_{\mathrm{pp}} = 0.92\,\mathrm{kV}$ is nearly strong enough to prevent LSB bursting, but random perturbations of the transition process can trigger LSB bursting at this forcing amplitude. For the leftmost run plotted in Fig. 9(c), there is a temporary reestablishment of increased suction indicative of LSB reformation with a duration of approximately $75c/u_\infty$ after t_i. However, the LSB bursts again at $tu_\infty/c \approx 380$. For $V_{\mathrm{pp}} = 1.41\,\mathrm{kV}$, increased suction within

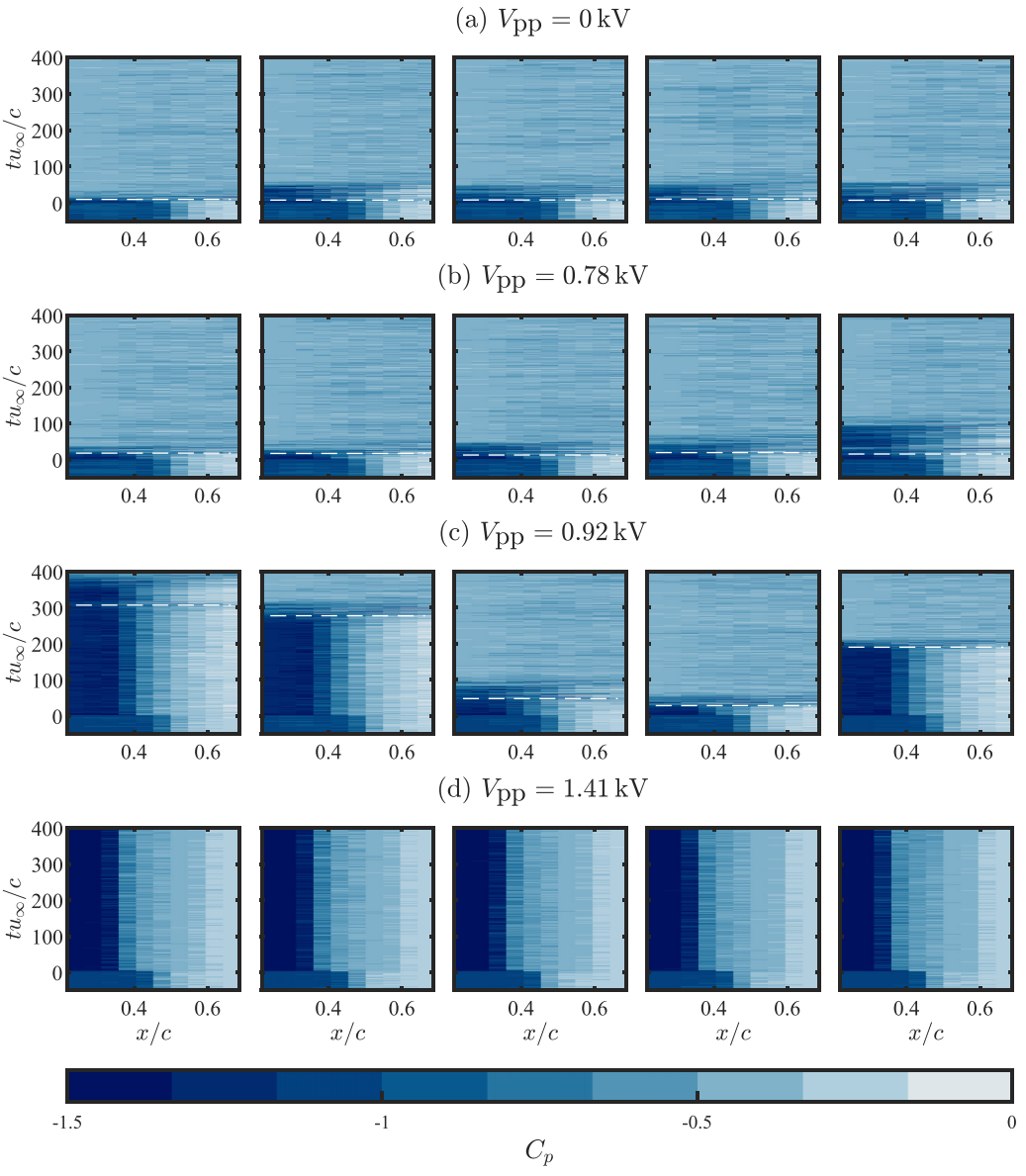


FIG. 9. Transient pressure coefficients on the suction surface of the airfoil for five selected runs at each amplitude of forcing. Dashed lines: t_i.

the LSB is maintained indefinitely for all runs, consistent with the pressure measurements for the limiting flow state in Fig. 5(i) that indicate the persistence of the LSB. The increase in suction within the LSB for the highest amplitude of forcing is greater than that in the unsustainable LSB that precedes bursting at $V_{\mathrm{pp}} = 0.92\,\mathrm{kV}$.

The pressure measurements indicate that with increasing forcing amplitude, the LSB bursting process is delayed on average and the LSB is likely to persist longer on the airfoil at the final angle of attack. Once a critical forcing amplitude is reached, which for this experimental setup is between $V_{\mathrm{pp}} = 0.92\,\mathrm{kV}$ and $1.41\,\mathrm{kV}$, bursting is entirely prevented. Although occasional reattachment was observed after LSB bursting at $V_{\mathrm{pp}} = 0.92\,\mathrm{kV}$, sustained oscillations between reattaching and massively separated flow states were not observed at any amplitude of forcing. When the forcing

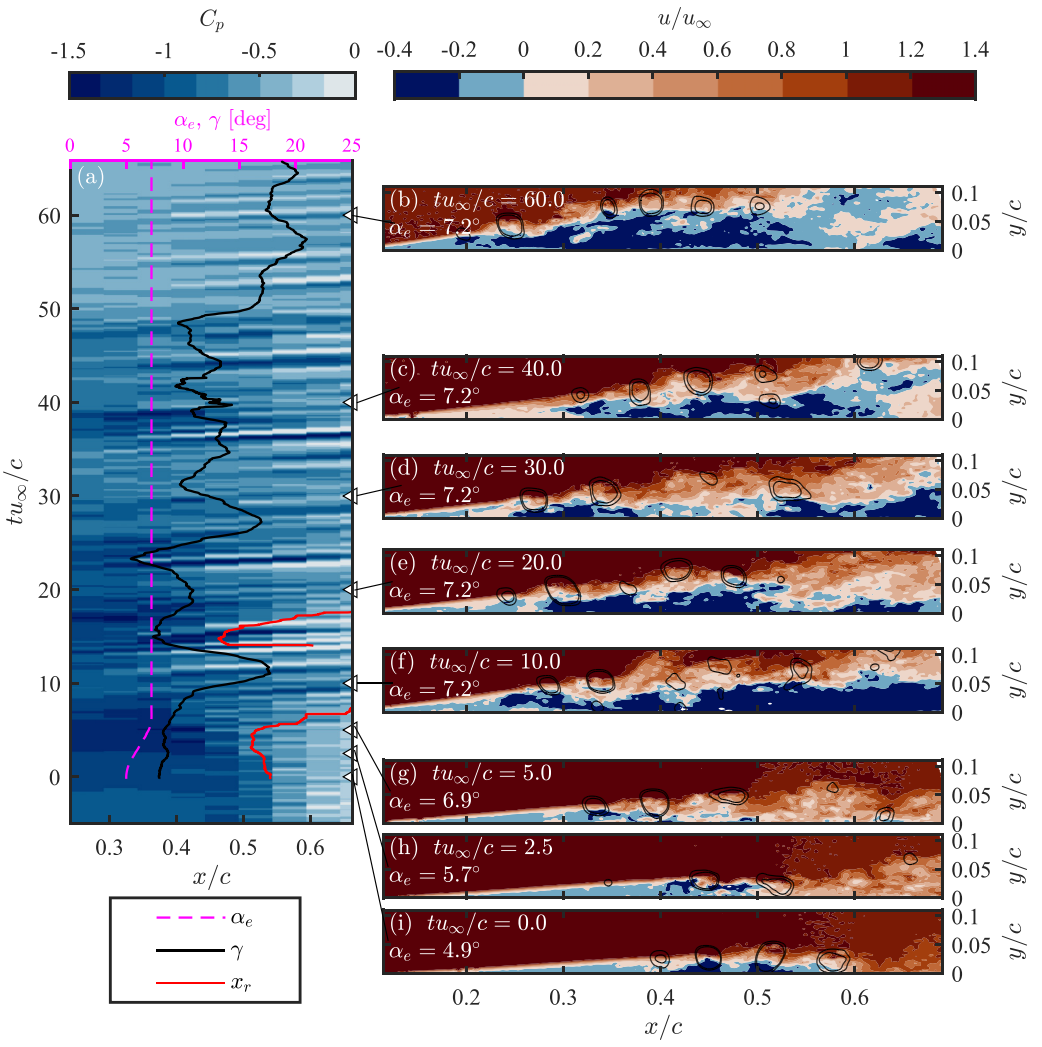


FIG. 10. Transient pressure coefficients (a) and streamwise velocity contours (b)–(i) on the suction surface of the airfoil during the pitch up motion for $V_{pp} = 0$. α_e: effective angle of attack, γ: separation angle, x_r: reattachment location, ◁: times of snapshots presented in panels (b)–(i), black contour lines: $\lambda_2 = -100u_\infty^2/c^2$ and $-200u_\infty^2/c^2$.

amplitude was insufficient to prevent bursting, the flow was observed to always progress toward a massively separated state. The irreversible progression of the flow toward a massively separated state after bursting is consistent with the stall hysteresis with respect to forcing amplitude reported by Benard *et al.* [20].

C. Transient flow-field development

The instantaneous flow-field development during the pitch up motion is explored in Fig. 10, which presents transient pressure measurements from the 10 pressure taps located on the suction surface together with velocity field measurements for a single trial with no forcing. After the beginning of the increase in angle of attack at $tu_\infty/c = 0$, there is a brief increase in suction within the LSB, and an upstream movement of the pressure rise associated with transition and reattachment. The reattachment point [red line in Fig. 10(a)] begins to rapidly move downstream when suction

within the LSB increases. Bursting of the LSB is followed by relatively large pressure fluctuations for $x/c > 0.35$. In the $tu_\infty/c - x/c$ plane, the pressure fluctuations appear as oblique structures. The low pressure oblique structures are likely caused by the shedding of large vortices from the separated shear layer that is expected to occur during LSB bursting, e.g., Refs. [14,20,60,62]. The average streamwise convective speed of these pressure fluctuations is estimated from their slopes to be $0.3u_\infty$. This is within the range of dynamic stall vortex convection speeds reported by [63]. This suggests that the shear layer mode of dynamic stall, in which multiple convectively growing vortices are shed from the leading edge shear layer [61], occurs for the conditions of this study. However, vortices corresponding to these pressure fluctuations could not be unambiguously identified in the PIV measurements. Because of the diagonal layout of the pressure taps on the suction surface, the PIV and surface pressure measurements were not taken at the same spanwise location. Therefore, low-frequency spanwise modulation of the separated flow may also contribute to the appearance of the oblique structures in the transient surface pressure measurements, e.g., Refs. [64,65], and spanwise vortex deformations may also reduce the coherence between PIV and surface pressure measurements. As the flow approaches the limiting massively separated condition, the amplitude of pressure fluctuations gradually decreases.

The corresponding flow-field development is illustrated in Figs. 10(b) to 10(i), which present contours of streamwise velocity and λ_2 criterion [66]. At $tu_\infty/c = 0.0$ [Fig. 10(i)], the laminar boundary layer separates at $x/c = 0.2$ and the separated shear layer rolls up into vortices near the location of transition at approximately $x/c = 0.45$. During the increase in angle of attack at $tu_\infty/c = 2.5$ [Fig. 10(h)], the location of shear layer roll-up moves upstream to approximately $x/c = 0.3$. As the end of the pitching motion is approached [Fig. 10(g)], the vortex roll-up location continues to move upstream and the turbulent shear layer increases in thickness. After the pitching motion is complete [Figs. 10(b) to 10(f)], relatively strong reverse flow is present over a majority of the suction surface. The separation angle of the laminar shear layer (γ), estimated from the standard PIV correlation method using a linear fit to the net-zero-streamwise mass-flux line upstream of $x/c = 0.3$, and averaged over a temporal window of $4c/u_\infty$, is plotted in Fig. 10(a). Beginning at $\gamma \approx 8^\circ$, the separation angle undergoes large oscillations for approximately 50 convective time units as it settles to its final position of $\gamma \approx 18^\circ$. The relatively larger size of vortices formed in the massively separated flow [for example, the vortex at $x/c \approx 0.3$ in Fig. 10(d)] may be responsible for the downstream convecting pressure fluctuations seen in Fig. 10(a) after LSB bursting. It is interesting to note that the local minima in separated shear layer angle that occur at $tu_\infty/c \approx 15$ and 23 are accompanied by relatively larger amplitude surface pressure fluctuations. This supports the assertion made earlier that the oblique ridges in Fig. 10(a) are caused by vortices formed in the separated shear layer, which produce larger surface pressure fluctuations when the separated shear layer is closer to the airfoil surface. After the initial cessation of reattachment, there is a period of temporary reattachment for $14 < tu_\infty/c < 18$. However, intermittent reattachment does not occur in the final limiting flow state where the flow remains massively separated. The unforced bursting process observed in the present study has a duration of approximately 50 convective time units, which is similar to the duration of LSB bursting transients previously reported by the authors during changes in Reynolds number and ramp type pitching motions in a different facility [67].

The streamwise flow development during a pitch up motion with periodic forcing at $V_{pp} = 0.92\,\text{kV}$ is illustrated in Fig. 11. The flow development during the bursting process is qualitatively similar to that observed in the unforced case, but the time at which the LSB bursts is substantially delayed relative to the end of the pitching motion, with the rapid downstream movement of the reattachment point and collapse of the pressure plateau occurring at $tu_\infty/c \approx 20$. In the unsustainable LSB that initially persists at $\alpha_e = 7.2^\circ$, vortex roll up occurs as far upstream as $x/c \approx 0.3$ [Figs. 11(e) to 11(f)] due to the stronger adverse pressure gradient at the final angle of attack, e.g., Ref. [53]. As in the unforced flow, the separated shear layer undergoes oscillations in its trajectory after LSB bursting, and relatively prominent local minima of the separation angle at $tu_\infty/c \approx 37$ and 45 are associated with higher amplitude surface pressure fluctuations.

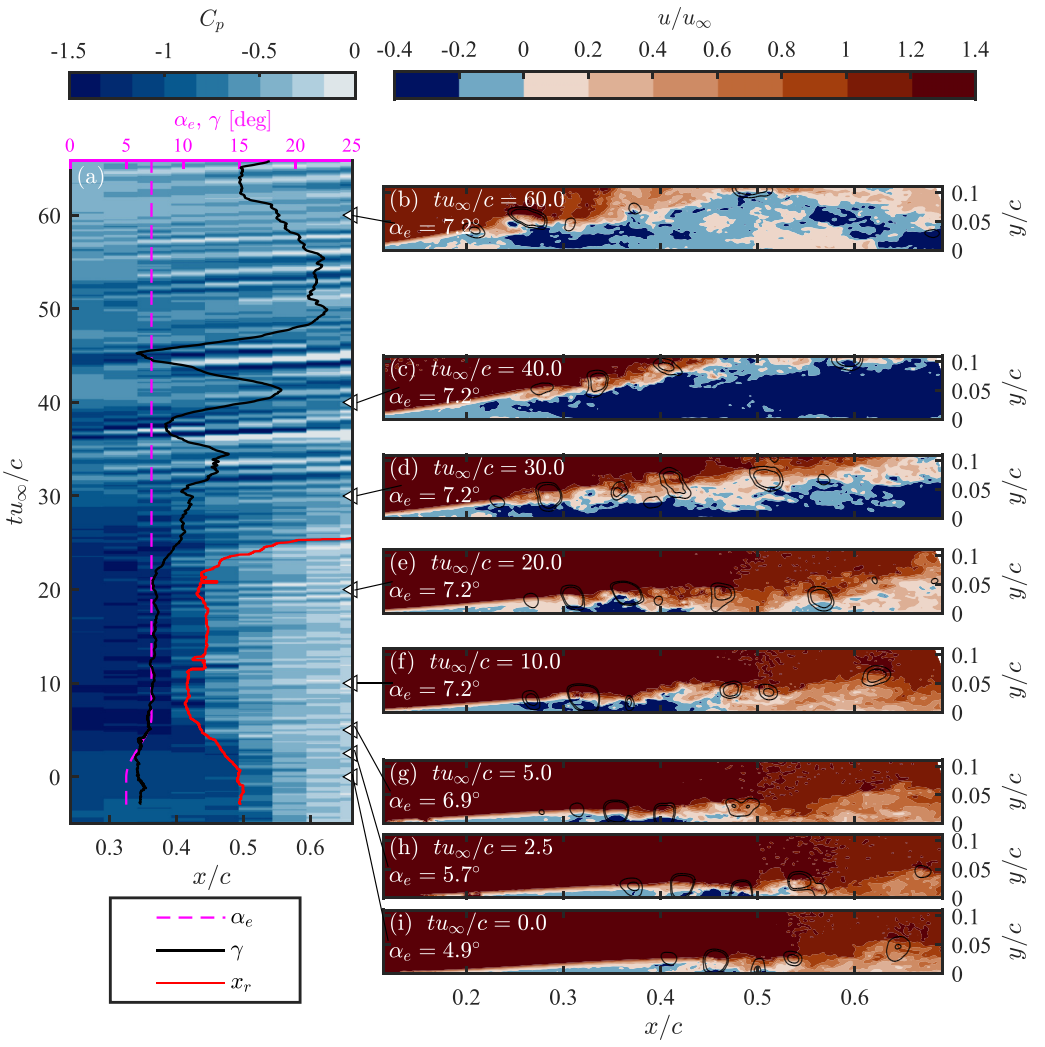


FIG. 11. Transient pressure coefficients (a) and streamwise velocity contours (b)–(i) on the suction surface of the airfoil during the pitch up motion for $V_{pp} = 0.92$. α_e: effective angle of attack, γ: separation angle, x_r: reattachment location, $\triangleleft$: times of snapshots presented in panels (b)–(i), black contour lines: $\lambda_2 = -100u_\infty^2/c^2$ and $-200u_\infty^2/c^2$.

A statistical comparison of the transient movement of the separation, transition and reattachment locations between forcing amplitudes is presented in Fig. 12. The separation location was estimated from velocity data obtained using the average correlation method over a temporal kernel of seven image pairs, whereas the other locations were estimated from the standard PIV correlation method. All three locations were estimated after applying a temporal moving average with a window length of $4c/u_\infty$ to the respective velocity field data. The solid lines in Fig. 12 are the ensemble-averages of the separation, transition, and reattachment locations for the times when they can be estimated for all five runs. The shaded areas are bounded by the ensemble minimum and maximum.

In the unforced flow [Fig. 12(a)], the increase in angle of attack leads to an initial upstream movement in the locations of separation and transition, consistent with the effect expected from a quasisteady change in angle of attack [33]. The reattachment point is relatively less affected during

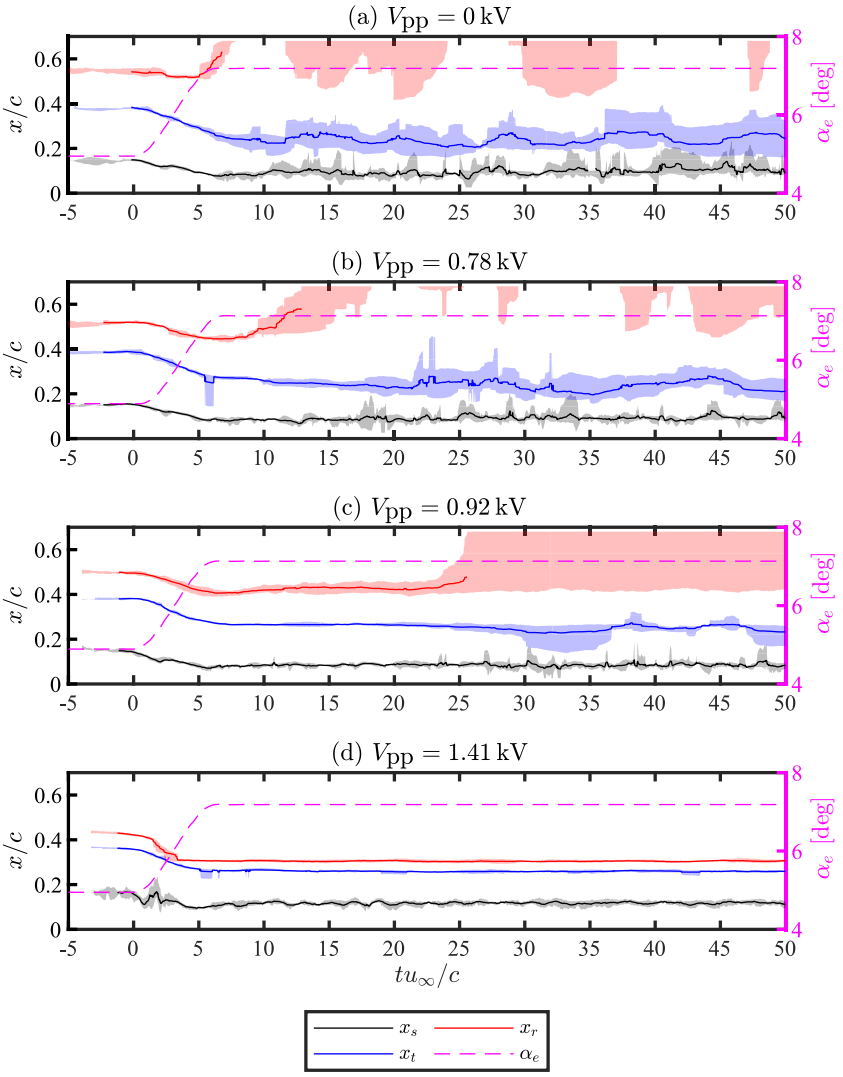


FIG. 12. Movement of ensemble-averaged separation (x_s), transition (x_t), and reattachment (x_t) locations. The areas between the ensemble minimum and maximum of each parameter are shaded. α_e: effective angle of attack.

the initial portion of the pitching motion. Near the end of the pitching motion, the adverse pressure gradient becomes sufficiently strong that a rapid downstream movement of the reattachment point occurs, and reattachment is no longer observed within the PIV field of view after $tu_\infty/c = 8$ for all five PIV recordings. After the initial downstream movement of the reattachment point, intermittent reattachment occurs due to the formation of large leading edge vortices and oscillations of the separated shear layer trajectory [cf. Fig. 10(d)]. This is reflected in the shaded red areas occurring after the initial cessation of reattachment that indicate the ensemble minimum reattachment location is within the PIV field of view. However, no intermittent reattachment was observed in the PIV measurements of the final limiting flow condition, which were recorded $380c/u_\infty$ after the start of the pitching motion. The gradual settling of the flow to a completely separated state is consistent with the reduction in pressure fluctuations for $tu_\infty/c > 100$ presented in Fig. 8(a).

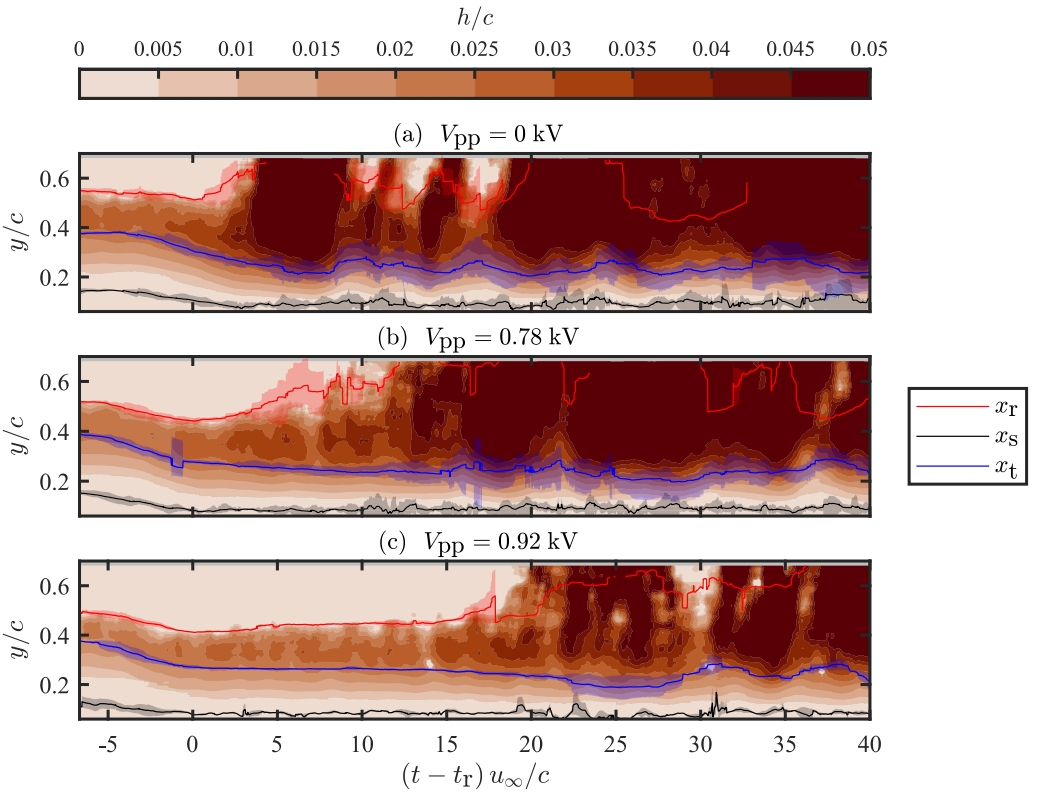


FIG. 13. Contours of the ensemble-averaged locus of zero-net-streamwise mass flux for runs where the LSB bursts and ensemble-averaged locations of separation, transition, and reattachment. Shaded areas are bounded by the ensemble minimum and maximum.

For $V_{pp} = 0.78$ kV [Fig. 12(b)] there is a significant upstream movement in the location of reattachment during the pitching motion, and the onset of the rapid downstream movement of the reattachment location is delayed to $tu_\infty/c \approx 10$. Before the reattachment location begins to move downstream, the length of the LSB is virtually unchanged compared to the initial limiting flow state. At the intermediate forcing amplitude of $V_{pp} = 0.92$ kV [Fig. 12(c)], the initial movement of the separation, transition, and reattachment locations is similar to that at the lowest forcing amplitude. However, reattachment persists at least until $tu_\infty/c = 25$ for the five runs recorded with PIV measurements. The length of the LSB that persists after the increase in angle of attack for $V_{pp} = 0.92$ kV is virtually unchanged relative to the LSB forming in the initial flow state. Although the length of the LSB prior to the downstream movement of reattachment is unchanged relative to the initial limiting flow state for $V_{pp} = 0.78$ kV and 0.92 kV, there is a 37% reduction in LSB length after the pitching motion for the highest amplitude of forcing for which the LSB does not burst [Fig. 12(d)].

A comparison of the LSB topology for runs for which the LSB bursts during or after the pitching motion and runs for which the LSB does not burst is facilitated by Figs. 13 and 14, respectively, which present contours of the ensemble-average locus of the zero-net-streamwise mass flux (h). This locus approximates the dividing streamline connecting the separation and reattachment points.

For the runs where the LSB bursts, the ensemble average was taken after shifting each run by the time when the reattachment location reaches its most upstream location (t_r) (Fig. 13). During these runs, the upstream movement of the separation, transition, and reattachment points that occurs during the pitching motion is accompanied by an increase in the maximum height of the LSB and

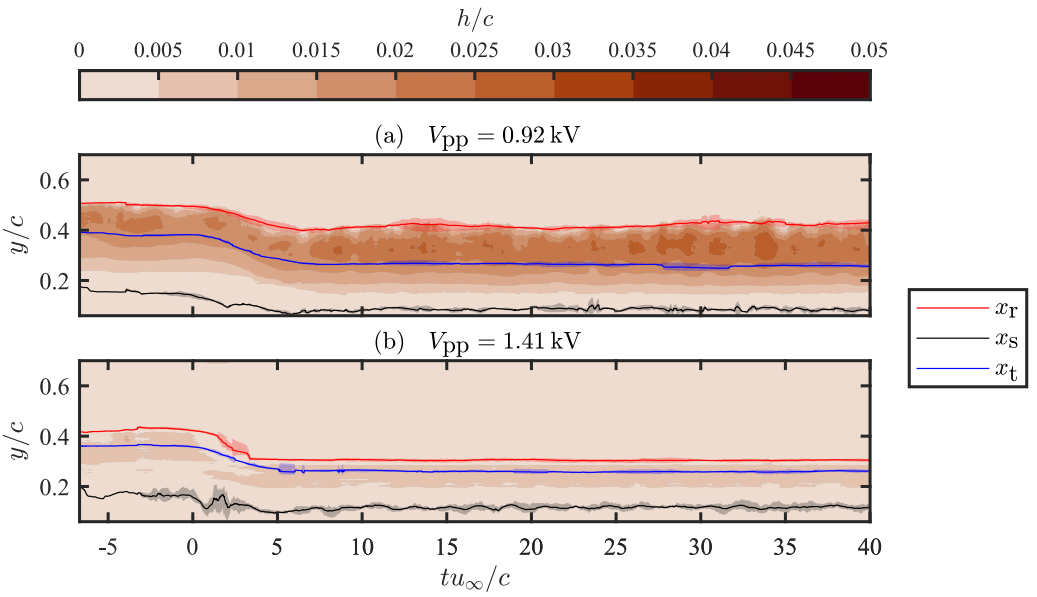


FIG. 14. Contours of the ensemble-averaged locus of zero-net-streamwise mass flux for runs where the LSB bursts and ensemble-averaged locations of separation, transition, and reattachment. Shaded areas are bounded by the ensemble minimum and maximum.

an upstream movement of the location of maximum height. For the case of $V_{pp} = 0\,kV$, the height of the LSB increases relatively rapidly after the moment when the ensemble-averaged reattachment point is farthest upstream ($t - t_r = 0$). For the runs with periodic forcing [Figs. 13(b) and 13(c)], the increase in LSB height becomes progressively more gradual with increasing forcing amplitude. During the period of gradual thickening of the LSB for $V_{pp} = 0.78\,kV$ and $0.92\,kV$, there is a gradual upstream movement in the location of transition, which is consistent with the expected effect of an increase in the distance of the separated shear layer from the airfoil surface [52]. The gradual thickening of the LSB and upstream movement of transition during this period suggests that the eventual bursting of the LSB is the result of a progressive enlargement of the recirculating flow region due to the inability of the flow within the boundary layer to overcome the adverse pressure gradient.

For the runs where the LSB did not burst, the ensemble averaged locus of the zero-net-streamwise mass flux was computed without applying a time shift to the data from individual runs (Fig. 14). For the three runs where the LSB did not burst within the PIV measurement period at a forcing amplitude of $V_{pp} = 0.92\,kV$, the LSB does not significantly increase in length or thickness after the pitching motion [Fig. 14(a)]. The transition location for these runs also remains largely unchanged after the pitching motion. Likewise, at the highest forcing amplitude for which LSB bursting did not occur for any of the runs, the size and position of the LSB remain virtually constant after the pitching motion [Fig. 14(b)]. Therefore, the progressive growth of the LSB at the final angle of attack in the runs where the LSB burst is a possible warning signal that could be used for the development of predictive LSB bursting criteria.

The transient changes in frequencies of wall-normal velocity fluctuations in the separated shear layer during the LSB bursting process were analysed using a continuous wavelet transform according to the procedure detailed in Sec. II E 2. A comparison of the time-frequency development of shear layer velocity fluctuations for runs for which the LSB bursts during or after the pitching motion and runs for which the LSB does not burst is facilitated by Figs. 15 and 16, respectively. Similar to Figs. 13 and 14, the ensemble-averaged wavelet magnitude scalograms in Fig. 15 have

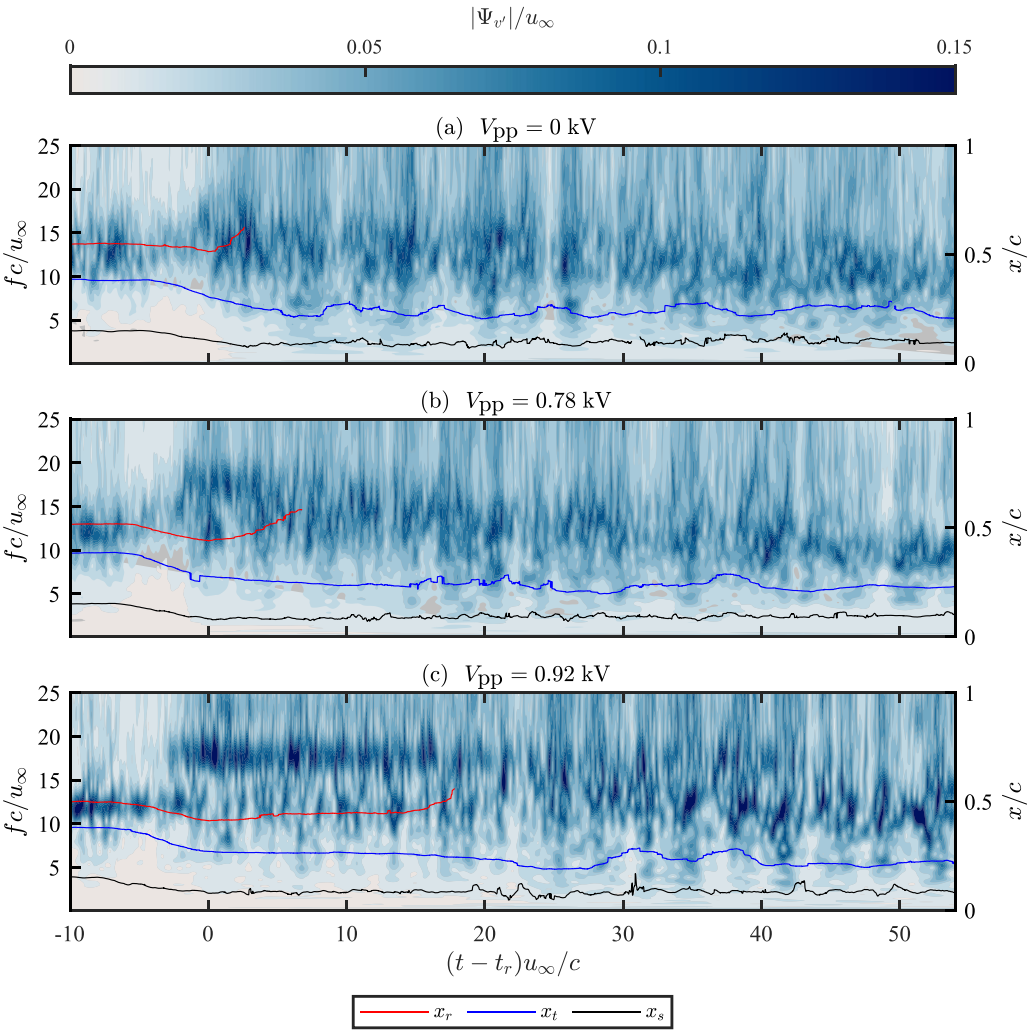


FIG. 15. Ensemble-averaged wavelet magnitude scalograms of wall-normal velocity fluctuations and ensemble-averaged locations of separation, transition, and reattachment for runs when the LSB burst.

been computed after shifting the data from each run by t_r, whereas no time shift was applied to the data in Fig. 16.

Because LSB bursting in the unforced flow occurs within eight convective time units of the start of the pitching motion, the angle of attack for all runs for the unforced flow at $(t - t_r)u_\infty/c = -10$ is equal to the initial angle of attack. In the unforced flow for $(t - t_r)u_\infty/c \leqslant -8$, the largest wavelet coefficient magnitudes are centered at $fc/u_\infty \approx 12$ [Fig. 15(a)], consistent with the band of amplified frequencies in the power spectrum of the initial limiting flow state for the unforced flow in Fig. 6(a). As the mean separation and transition locations move upstream during the increase in angle of attack, the largest amplitude wall-normal velocity fluctuations largely remain within $4 \leqslant fc/u_\infty \leqslant 18$. After the cessation of reattachment, there is a gradual decrease in the frequency of the largest amplitude wall-normal velocity fluctuations, with the highest amplitude fluctuations at $(t - t_r)u_\infty/c = 50$ centered at a frequency of approximately $fc/u_\infty = 9$.

For the two forcing amplitudes that are insufficient to prevent bursting [Figs. 15(b) and 15(c)], the final angle of attack is reached before expansion of the LSB begins. At the final angle of attack,

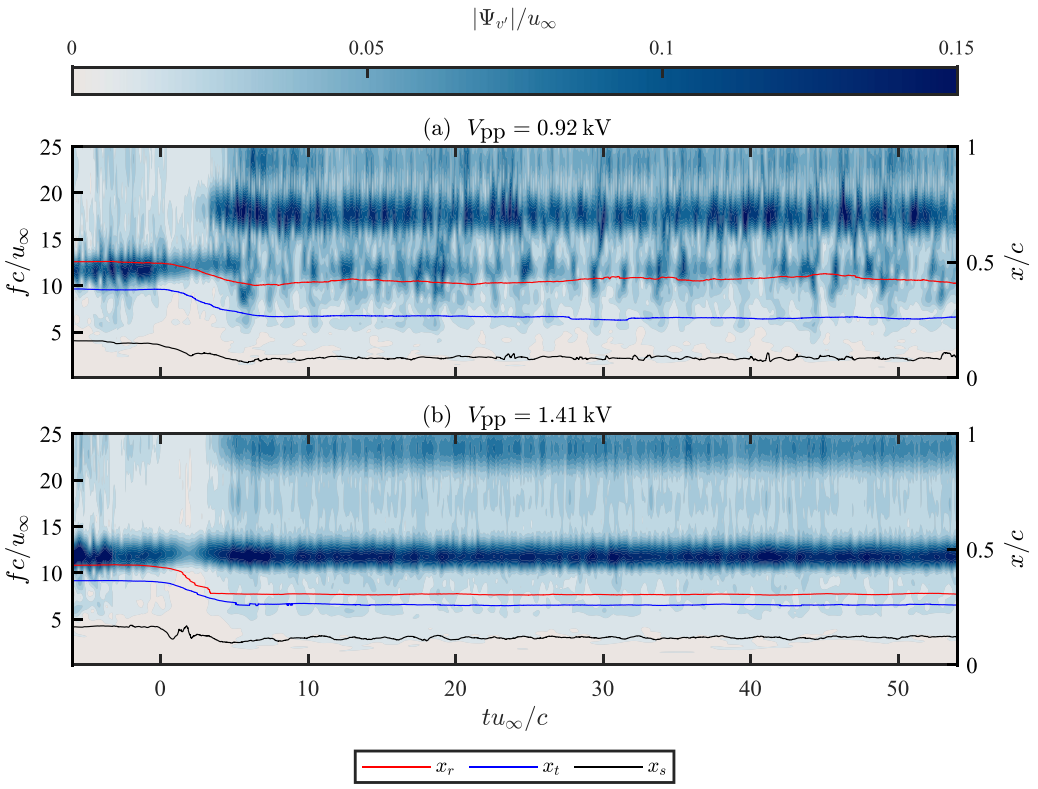


FIG. 16. Ensemble-averaged wavelet magnitude scalograms of wall-normal velocity fluctuations and ensemble-averaged locations of separation, transition, and reattachment for runs when the LSB did not burst within the PIV measurement period.

there are substantial velocity fluctuations at a frequency of $fc/u_\infty \approx 17.5$ before the cessation of reattachment, consistent with the expected increase in the most amplified frequency in the separated shear layer due to an increase in angle of attack [68]. After the cessation of reattachment, there is a gradual reduction in the most amplified frequency that occurs over a time period on the order of $50c/u_\infty$, similar to the unforced flow. The gradual decrease in the most amplified frequency after LSB bursting in unforced and forced conditions suggests that the stability characteristics of the separated shear layer are largely insensitive to the presence or absence of reattachment. Instead, the progressive decrease in the velocity difference across the shear layer, driven primarily by the reduction in velocity of the outer flow following LSB bursting, causes a gradual reduction in the most amplified frequency. This conclusion is consistent with the ensemble-averaged surface pressure distributions in Figs. 8(b), 8(d), and 8(f), since the reduction in suction that follows bursting occurs over a period of approximately $30c/u_\infty$, implying a corresponding time-scale for the reduction in the velocity of the outer flow.

For the three runs at a forcing amplitude of $V_{\mathrm{pp}} = 0.92\,\mathrm{kV}$ where the LSB does not burst within the PIV measurement period, relatively strong wall-normal velocity fluctuations centered at $fc/u_\infty \approx 17.5$ are maintained after the LSB moves upstream during the pitching motion [Fig. 16(a)]. This suggests that nonlinear effects are important for delaying the bursting of the LSB. However, when the forcing amplitude is sufficient to prevent bursting entirely, wall-normal velocity fluctuations at the forcing frequency dominate in the initial and final limiting flow states [Fig. 15(d)], indicating that the amplitudes of the forced disturbances overwhelm the higher frequencies that are

expected to be amplified by the separated shear layer. There are also substantial fluctuations at the first harmonic of the forcing frequency ($fc/u_\infty = 23.4$) at the highest forcing amplitude.

D. Effect of forcing amplitude on the initial conditions of bursting

Since the possibility of reattachment of the separated shear layer depends on the strength of the adverse pressure gradient and the ability of the shear layer to transition, the transient flow development was investigated in terms of pressure gradient and shear layer instability using the LSB bursting criterion of Gaster [8]. This criterion quantifies the adverse pressure gradient using the parameter $P = \theta_s^2/\nu(\Delta u_e/\Delta x)$, where $\theta_s = \int_0^\delta (u/u_e)(1-(u/u_e))dy$ is the momentum thickness at the separation point, ν is the kinematic viscosity, and $\Delta u_e/\Delta x$ is the mean edge velocity gradient between the locations of x_s and x_r in a hypothetical fully attached flow. The value of P at which LSBs burst is correlated with the momentum thickness Reynolds number at the separation point ($\mathrm{Re}_{\theta_s} = u_{e,s}\theta_s/\nu$) which provides an indication of the degree of instability of the laminar shear layer. Higher Re_{θ_s} indicates greater instability and implies a tendency for the shear layer to transition more rapidly, e.g., Ref. [69]. Although the bursting criterion of Gaster [8] is not necessarily applicable to transient conditions, Re_{θ_s} and P are physically meaningful parameters that provide insight into the evolution of the LSB during the pitching transient.

The pressure gradient parameter P in the bursting criterion of [8] is analogous to the nondimensional pressure gradient parameter $m = (\theta^2/\nu)(\partial u_e/\partial x)$ used by Thwaites [70] to predict the separation of laminar boundary layers. Using the pressure gradient parameter P as an analog of m facilitates the investigation of separating-reattaching flows under a similar paradigm. Since Re_{θ_s} and P both depend on θ and u_e, the manner by which Re_{θ_s} and P vary during a change in operating conditions is not trivial [8].

Figures 17(a) and 17(b) present the time-histories of Re_{θ_s} and P for the five runs recorded with PIV at each amplitude of forcing, respectively. The velocity field data used to calculate Re_{θ_s} and P was averaged over a sliding temporal window of $4c/u_\infty$ for better statistical convergence. For the runs where bursting occurs, the data are plotted up to the time that reattachment ceases. In this work, $\Delta u_e/\Delta x$ was estimated from the inviscid edge velocity distribution over the airfoil calculated using the XFOIL software [37]. In the limiting flow state prior to the pitching motion, the initial value of Re_{θ_s} for the two highest forcing amplitudes is higher than those for the unforced flow and lowest forcing amplitude. Because θ is related to the momentum flux deficit in the boundary layer, the increase in Re_{θ_s} for the higher forcing amplitudes is attributed to greater friction drag and boundary layer edge velocity upstream of separation when the LSB thickness is reduced at higher forcing amplitudes. However, the difference in initial Re_{θ_s} between the two highest forcing amplitudes is not significant, suggesting that further increases in forcing amplitude would have a relatively minor effect on Re_{θ_s}.

During the initial portion of the pitch up motion, there is a transient decrease in Re_{θ_s} and increase in P [Figs. 17(a) and 17(b)] caused by a transient decrease in θ_s [Fig. 17(c)]. This transient decrease in θ_s is likely due to the moving wall effect [15] during the pitching motion, which decreases the momentum deficit in the boundary layer near the leading edge. In the unforced flow, the values of Re_{θ_s} and P tend to decrease toward the end of the pitching motion. These changes are consistent with the reduction in boundary layer edge velocity and downstream movement of the reattachment location that occur during bursting. As the amplitude of periodic forcing is increased, there is a tendency for higher values of Re_{θ_s} and P to persist after the end of the pitching motion. This suggests that there is a decrease in shear layer stability and that a stronger adverse pressure gradient is maintained after the end of the pitching motion when the forcing amplitude is increased. However, for runs where the LSB bursts within the PIV measurement period, a decrease in Re_{θ_s} and P is observed prior to cessation of reattachment. For example, at $V_{pp} = 0.92\,\mathrm{kV}$ there are two runs where reattachment ceases at $tu_\infty/c = 26$ and 30, respectively. Although there are large oscillations in Re_{θ_s} and P, these runs exhibit reduced Re_{θ_s} and P prior to bursting relative to the runs at this forcing amplitude where the LSB did not burst. This suggests that a decrease in Re_{θ_s} and P could be used as

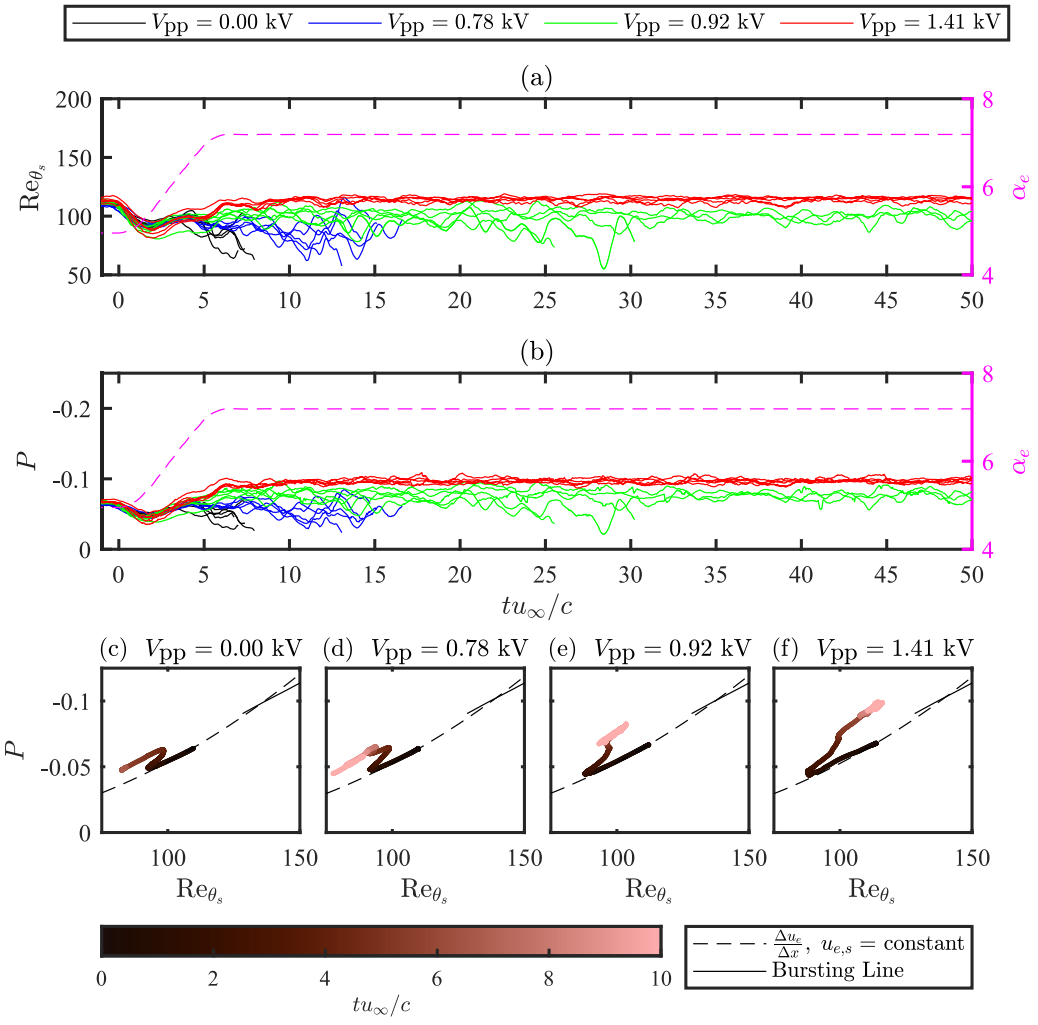


FIG. 17. $P - \mathrm{Re}_{\theta_s}$ trajectory.

an indication of impending LSB bursting. When the amplitude of the periodic forcing is sufficiently strong to prevent LSB bursting entirely ($V_{pp} = 1.41$ kV), Re_{θ_s} largely returns to its initial value after the pitching motion, and a stronger adverse pressure gradient relative to the other forcing amplitudes is maintained.

The ensemble-averaged values of P are plotted against Re_{θ_s} for each forcing amplitude in Figs. 17(c) to 17(f). The solid line in the plots is the bursting line. According to Gaster [8], bursting occurs when an LSB moves from the short-bubble region below the bursting line to the long-bubble region above the bursting line. As expected for the short LSBs forming on the airfoil at the high prestall angle of attack of the initial limiting flow state, the initial LSBs for all forcing levels are relatively close to an extrapolation of the bursting line to lower Re_{θ_s}. The transient decrease in θ_s that occurs during the pitching motion results in a movement of the LSB toward the lower left in the $\mathrm{Re}_{\theta_s} - P$ plane. The dashed line in Figs. 17(d) to 17(g) is the trajectory that the LSB would take if $\Delta u_e/\Delta x$ and $u_{e,s}$ remained constant at their initial values during the change in θ_s. Since the observed trajectories lie to the upper left of the dashed line, the corresponding changes in Re_{θ_s} and P are not entirely attributable to the change in θ_s. Instead, the change in LSB location and angle of attack during the pitching motion leads to a gradual movement of the LSB farther into the long

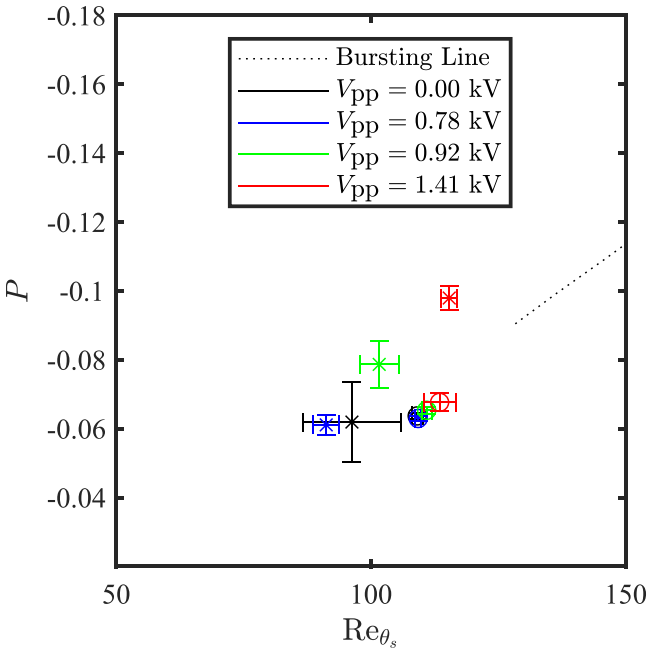


FIG. 18. Bursting criterion parameters of initial LSB (○) and LSB when the reattachment location is most upstream (×). Errorbars denote uncertainty (95% confidence) based on the variance of individual runs.

bubble region than would result simply from a change in θ_s. From Fig. 17(b) and Figs. 17(c)–17(f), it is apparent that higher forcing amplitudes enable the LSB to persist at more negative values of P. Therefore, the effect of periodic forcing can be considered as a shift of the bursting line to more negative values of P at a given Re_{θ_s}.

To further examine how the forcing amplitude affects the conditions under which LSB bursting initiates, the values of Re_{θ_s} and P are plotted for each forcing amplitude in Fig. 18. The results are presented for the point in time when the ensemble-averaged reattachment location reaches its most upstream position, which enables a comparison of the LSBs at the moment when they begin to expand and burst for different forcing amplitudes. The initial states of the LSBs at the initial angle of attack are also plotted for reference. Although there are notable differences in mean flow development in the initial flow state (Fig. 4), the initial location of the LSB in the $\mathrm{Re}_{\theta_s} - P$ plane is insensitive to forcing amplitude. However, periodic forcing leads to more substantial differences in the LSBs at the moment when they begin to expand. For the unforced LSB and the lowest amplitude of forcing ($V_{pp} = 0.78\,\mathrm{kV}$), the pressure gradient remains largely unchanged as the LSB contracts while there is a decrease in Re_{θ_s}. For $V_{\mathrm{pp}} = 0.92\,\mathrm{kV}$ and $1.41\,\mathrm{kV}$, there is a significant increase in P relative to $V_{\mathrm{pp}} = 0\,\mathrm{kV}$ and $0.78\,\mathrm{kV}$ when the reattachment point is at its most upstream location. For the two highest amplitudes of forcing, the LSB persists at least temporarily in the long-bubble region. This suggests that the adverse pressure gradient required to trigger bursting is effectively increased by the application of periodic forcing.

IV. CONCLUDING REMARKS

Wind tunnel experiments were performed on a NACA 0018 airfoil equipped with a spanwise-uniform AC-DBD plasma actuator for periodic forcing at the leading edge. The airfoil underwent ramp changes in effective angle of attack from $\alpha_e = 4.9^\circ$ to 7.2° at a mean nondimensional pitch rate of $\dot{\alpha}c/(2u_\infty) = 0.008$. Surface pressure measurements for an ensemble of 20 trials and

time-resolved PIV measurements for an ensemble of five trials were obtained for the unforced flow and at three amplitudes of periodic forcing. Forcing at the highest amplitude prevented LSB bursting entirely, whereas LSB bursting occurred in the unforced flow and for the two lowest forcing amplitudes.

In the unforced flow, the pitch up motion caused an upstream movement of the separation and shear layer roll-up locations and an increase in suction within the LSB. However, the reattachment point moved downstream during the change in angle of attack, and the LSB burst within $10c/u_\infty$ of the onset of the pitching motion. Periodic forcing caused a reduction in the length and thickness of the LSB at the initial angle of attack that was greater for higher forcing amplitudes. With periodic forcing, a significant upstream movement of the reattachment point occurred during the pitch up motion. Application of periodic forcing at amplitudes insufficient to prevent LSB bursting caused a delay in the mean bursting start time relative to the unforced flow, and the delay increased when the forcing amplitude was increased. The variance of the bursting start time also increased with forcing amplitude. However, the measured increase in bursting transient duration with forcing amplitude was not statistically significant, and similar transient flow field development was observed during LSB bursting at different forcing amplitudes.

In all cases, bursting involved a rapid downstream movement of the reattachment location, resulting in an extension of the pressure plateau. This was followed by a gradual decrease in suction, occurring over a period of approximately $30c/u_\infty$ and accompanied by a gradual decrease in the most amplified frequency in the separated shear layer. As the flow settled to the massively separated final state, relatively large fluctuations in suction surface pressure and separation angle gradually diminished in amplitude.

At the highest amplitude of forcing, the initial LSB at $\alpha_e = 4.9^\circ$ was reduced in length by 58% relative to the unforced flow, and bursting did not occur when the angle of attack was increased to $\alpha_e = 7.2^\circ$. In this case, the most amplified velocity fluctuations in the separated shear layer were locked to the forcing frequency at similar amplitudes in both the initial and final limiting flow states. The LSB persisted indefinitely after the pitch up motion, despite the expected change in shear layer stability characteristics with increasing angle of attack. This result demonstrates that maintaining the LSB and preventing massive separation during a transient change in operating conditions does not require modulation of the forcing frequency if the forcing amplitude is sufficiently high.

According to the two-parameter bursting criterion of Gaster [8], the LSB forming on the airfoil in the initial limiting flow state at $\alpha_e = 4.9^\circ$ was near the bursting line at all forcing amplitudes. The pitch up motion caused a movement of the location of the LSB in the $\mathrm{Re}_{\theta_s} - P$ plane that depended on forcing amplitude. In unforced conditions, Re_{θ_s} decreased during the pitching motion, and the LSB burst nearly immediately after reaching the final angle of attack. At higher forcing amplitudes insufficient to prevent bursting, the LSB persisted temporarily in the long-bubble region under an increased adverse pressure gradient before bursting. At the highest forcing amplitude, the LSB persisted indefinitely in the long-bubble region. This suggests that periodic forcing increases the nondimensional pressure gradient that the LSB is able to overcome without bursting at a given Reynolds number.

At all forcing amplitudes where it occurred, LSB bursting was an irreversible process. Although intermittent reattachment was observed after the initial cessation of reattachment and before the flow settled to a statistically stationary final state, the flow always progressed from a configuration with an LSB toward a configuration with massive separation. This irreversibility is attributed to the hysteresis of the stability characteristics of the separated laminar shear layer, e.g., Ref. [20]. Although forcing at the most amplified frequency of the separated laminar shear layer can delay or prevent LSB bursting, if the amplitude of forcing is insufficient to maintain reattaching flow, the forcing has negligible effect on the flow after bursting has occurred. For forcing amplitudes that are near the amplitude threshold required to maintain reattachment, when random external perturbations cause bursting, the forcing becomes incapable of returning the flow to a reattaching state. In contrast, naturally developing flows over airfoils at low Reynolds numbers near stall can experience spontaneous low-frequency oscillation between reattaching and massively separated

conditions, e.g., Ref. [71]. The absence of spontaneous reattachment when an LSB is subject to convectively amplified forced disturbances such as those introduced by the plasma actuator in the present study suggests that the spontaneous LSB formation observed in certain conditions is the result of an absolute rather than convective instability, in agreement with previous studies, e.g., Refs. [71,72].

ACKNOWLEDGMENTS

We acknowledge the support of the Natural Sciences and Engineering Research Council of Canada (NSERC). The authors express gratitude to S. Bernardy and E. Langedijk for their technical support. The scientific color maps berlin and vik [73] are used to prevent visual distortion of the data and exclusion of readers with color-vision deficiencies [74].

DATA AVAILABILITY

The data that support the findings of this article are not publicly available upon publication because it is not technically feasible and/or the cost of preparing, depositing, and hosting the data would be prohibitive within the terms of this research project. The data are available from the authors upon reasonable request.

[1] P. B. S. Lissaman, Low-Reynolds-number airfoils, Annu. Rev. Fluid Mech. **15**, 223 (1983).
[2] A. R. Jones, O. Cetiner, and M. J. Smith, Physics and modeling of large flow disturbances: Discrete gust encounters for modern air vehicles, Annu. Rev. Fluid Mech. **54**, 469 (2022).
[3] D. H. Wood, in *Advances in Wind Energy Conversion Technology* (Springer-Verlag, Berlin, Heidelberg, 2011), pp. 195–211.
[4] I. Tani, Low-speed flows involving bubble separations, Prog. Aerosp. Sci. **5**, 70 (1964).
[5] S. S. Diwan and O. N. Ramesh, On the origin of the inflectional instability of a laminar separation bubble, J. Fluid Mech. **629**, 263 (2009).
[6] S. Hosseinverdi and H. F. Fasel, Numerical investigation of laminar-turbulent transition in laminar separation bubbles: The effect of free-stream turbulence, J. Fluid Mech. **858**, 714 (2019).
[7] H. P. Horton, Laminar separation bubbles in two and three dimensional incompressible flow, Ph.D. thesis, University of London, London, UK, 1968.
[8] M. Gaster, The structure and behaviour of laminar separation bubbles, Technical Report, Reports and Memoranda 3595, Aeronautical Research Council, London, UK, 1967.
[9] S. Yarusevych and M. Kotsonis, Steady and transient response of a laminar separation bubble to controlled disturbances, J. Fluid Mech. **813**, 955 (2017).
[10] O. Marxen and D. S. Henningson, The effect of small-amplitude convective disturbances on the size and bursting of a laminar separation bubble, J. Fluid Mech. **671**, 1 (2011).
[11] M. R. Visbal and S. I. Benton, Exploration of high-frequency control of dynamic stall using large-eddy simulations, AIAA J. **56**, 2974 (2018).
[12] S. I. Benton and M. R. Visbal, The onset of dynamic stall at a high, transitional Reynolds number, J. Fluid Mech. **861**, 860 (2019).
[13] L. Damiola, M. F. Siddiqui, M. C. Runacres, and T. De Troyer, Influence of free-stream turbulence intensity on static and dynamic stall of a NACA 0018 aerofoil, J. Wind Eng. Ind. Aerodyn. **232**, 105270 (2023).
[14] J. Kern, D. Blanco, A. Cavalieri, P. Negi, A. Hanifi, and D. Henningson, Direct numerical simulations of an airfoil undergoing dynamic stall at different background disturbance levels, J. Fluid Mech. **986**, A3 (2024).

[15] L. E. Ericsson and J. P. Reding, Fluid mechanics of dynamic stall part I. Unsteady flow concepts, J. Fluids Struct. **2**, 1 (1988).
[16] A. Nati, R. de Kat, F. Scarano, and B. W. van Oudheusden, Dynamic pitching effect on a laminar separation bubble, Exp. Fluids **56**, 172 (2015).
[17] N. Alferez, I. Mary, and E. Lamballais, Study of stall development around an airfoil by means of high fidelity large eddy simulation, Flow, Turbul. Combust. **91**, 623 (2013).
[18] M. L. Post and T. C. Corke, Separation control using plasma actuators: Dynamic stall vortex control on oscillating airfoil, AIAA J. **44**, 3125 (2006).
[19] T. C. Corke, P. O. Bowles, C. He, and E. H. Matlis, Sensing and control of flow separation using plasma actuators, Philos. Trans. R. Soc. A **369**, 1459 (2011).
[20] N. Benard, L. N. Cattafesta, E. Moreau, J. Griffin, and J. P. Bonnet, On the benefits of hysteresis effects for closed-loop separation control using plasma actuation, Phys. Fluids **23**, 083601 (2011).
[21] M. Sato, T. Nonomura, K. Okada, K. Asada, H. Aono, A. Yakeno, Y. Abe, and K. Fujii, Mechanisms for laminar separated-flow control using dielectric-barrier-discharge plasma actuator at low Reynolds number, Phys. Fluids **27**, 117101 (2015).
[22] S. Yarusevych, P. E. Sullivan, and J. G. Kawall, On vortex shedding from an airfoil in low-Reynolds-number flows, J. Fluid Mech. **632**, 245 (2009).
[23] M. Karp and M. J. Hack, Optimal suppression of a separation bubble in a laminar boundary layer, J. Fluid Mech. **892**, A23 (2020).
[24] S. Yarusevych and M. Kotsonis, Effect of local DBD plasma actuation on transition in a laminar separation bubble, Flow Turbul. Combust. **98**, 195 (2017).
[25] D. Borgmann, J. Little, and H. Fasel, Active control of transition to turbulence in laminar separation bubbles, J. Fluid Mech. **1016**, A59 (2025).
[26] D. Greenblatt and I. J. Wygnanski, The control of flow separation by periodic excitation, Prog. Aerosp. Sci. **36**, 487 (2000).
[27] T. Michelis, S. Yarusevych, and M. Kotsonis, On the origin of spanwise vortex deformations in laminar separation bubbles, J. Fluid Mech. **841**, 81 (2018).
[28] B. L. Ramos, W. R. Wolf, C. A. Yeh, and K. Taira, Active flow control for drag reduction of a plunging airfoil under deep dynamic stall, Phys. Rev. Fluids **4**, 074603 (2019).
[29] O. Marxen, M. Lang, and U. Rist, Vortex formation and vortex breakup in a laminar separation bubble, J. Fluid Mech. **728**, 58 (2013).
[30] C. E. Toppings and S. Yarusevych, Transient dynamics of laminar separation bubble formation and bursting, Exp. Fluids **64**, 57 (2023).
[31] J. J. Wang, K. S. Choi, L. H. Feng, T. N. Jukes, and R. D. Whalley, Recent developments in DBD plasma flow control, Prog. Aerosp. Sci. **62**, 52 (2013).
[32] R. Merino-Martínez, A. Rubio Carpio, L. T. Lima Pereira, S. van Herk, F. Avallone, D. Ragni, and M. Kotsonis, Aeroacoustic design and characterization of the 3D-printed, open-jet, anechoic wind tunnel of Delft University of Technology, Appl. Acoust. **170**, 107504 (2020).
[33] M. S. H. Boutilier and S. Yarusevych, Effects of end plates and blockage on low-Reynolds-number flows over airfoils, AIAA J. **50**, 1547 (2012).
[34] T. A. Fox and G. S. West, On the use of end plates with circular cylinders, Exp. Fluids **9**, 237 (1990).
[35] Y. Zhang, F. Avallone, and S. Watson, Wind turbine blade trailing edge crack detection based on airfoil aerodynamic noise: An experimental study, Appl. Acoust. **191**, 108668 (2022).
[36] W. H. Rae and A. Pope, *Low-Speed Wind Tunnel Testing*, 1st ed (John Wiley & Sons, New York, NY, 1966).
[37] M. Drela, in XFOIL: An analysis and design system for low Reynolds number airfoils, in *Low Reynolds Number Aerodynamics*, edited by T. J. Mueller (Springer, Berlin, Heidelberg, 1989), pp. 1–12.
[38] S. A. Whitmore and M. D. Wilson, Wiener deconvolution for reconstruction of pneumatically attenuated pressure signals, AIAA J. **49**, 890 (2011).
[39] B. Wieneke, PIV uncertainty quantification from correlation statistics, Meas. Sci. Technol. **26**, 074002 (2015).
[40] A. Sciacchitano and B. Wieneke, PIV uncertainty propagation, Meas. Sci. Technol. **27**, 084006 (2016).

[41] R. J. Moffat, Describing the uncertainties in experimental results, Exp. Therm Fluid Sci. **1**, 3 (1988).
[42] C. D. Meinhart, S. T. Wereley, and J. G. Santiago, A PIV algorithm for estimating time-averaged velocity fields, J. Fluids Eng. **122**, 285 (2000).
[43] D. E. Ashpis and M. C. Laun, Dielectric barrier discharge (DBD) plasma actuators thrust - measurement methodology incorporating new anti-thrust hypothesis, in *Proceedings of the 52nd Aerospace Sciences Meeting* (American Institute of Aeronautics and Astronautics, Reston, VA, 2014), pp. 1–16.
[44] A. V. Boiko, G. R. Grek, A. V. Dovgal, and V. V. Kozlov, *The Origin of Turbulence in Near-Wall Flows* (Springer, Berlin, Heidelberg, 2002), Vol. 7.
[45] M. Ol, B. McCauliffe, E. Hanff, U. Scholz, and C. J. Kähler, Comparison of laminar separation bubble measurements on a low Reynolds number airfoil in three facilities, in *Proceedings of the 35th AIAA Fluid Dynamics Conference and Exhibit* (American Institute of Aeronautics and Astronautics, Reston, Virigina, 2005).
[46] R. Hain, C. J. Kähler, and R. Radespiel, Dynamics of laminar separation bubbles at low-Reynolds-number aerofoils, J. Fluid Mech. **630**, 129 (2009).
[47] J. M. Lilly and S. C. Olhede, Generalized morse wavelets as a superfamily of analytic wavelets IEEE Trans. Signal Process. **60**, 6036 (2012).
[48] J. M. Lilly, Element analysis: A wavelet-based method for analysing time-localized events in noisy time series, Proc. R. Soc. A **473**, 20160776 (2017).
[49] A. Grille Guerra, C. Mertens, J. Little, and B. van Oudheusden, Experimental characterization of an unsteady laminar separation bubble on a pitching wing, Exp. Fluids **64**, 16 (2023).
[50] S. S. Diwan and O. N. Ramesh, Relevance of local parallel theory to the linear stability of laminar separation bubbles, J. Fluid Mech. **698**, 468 (2012).
[51] R. Gerakopulos and S. Yarusevych, Novel time-resolved pressure measurements on an airfoil at a low Reynolds number, AIAA J. **50**, 1189 (2012).
[52] A. Dovgal, V. Kozlov, and A. Michalke, Laminar boundary layer separation: Instability and associated phenomena, Prog. Aerosp. Sci. **30**, 61 (1994).
[53] M. S. H. Boutilier and S. Yarusevych, Parametric study of separation and transition characteristics over an airfoil at low Reynolds numbers, Exp. Fluids **52**, 1491 (2012).
[54] D. Lengani, D. Simoni, M. Ubaldi, and P. Zunino, POD analysis of the unsteady behavior of a laminar separation bubble, Exp. Therm Fluid Sci. **58**, 70 (2014).
[55] P. Welch, The use of fast Fourier transform for the estimation of power spectra: A method based on time averaging over short, modified periodograms, IEEE Trans. Audio Electroacoust. **15**, 70 (1967).
[56] J. W. Kurelek, S. Yarusevych, and M. Kotsonis, Vortex merging in a laminar separation bubble under natural and forced conditions, Phys. Rev. Fluids **4**, 063903 (2019).
[57] O. Marxen and U. Rist, Mean flow deformation in a laminar separation bubble: Separation and stability characteristics, J. Fluid Mech. **660**, 37 (2010).
[58] S. Pröbsting and S. Yarusevych, Laminar separation bubble development on an airfoil emitting tonal noise, J. Fluid Mech. **780**, 167 (2015).
[59] C. E. Toppings and S. Yarusevych, Laminar separation bubble formation and bursting on a finite wing, J. Fluid Mech. **986**, A26 (2024).
[60] W. J. McCroskey, The phenomenon of dynamic stall, Technical Report NASA-TM-81264, NASA Ames Research Center, Moffat Field, CA, 1981.
[61] K. Mulleners and M. Raffel, Dynamic stall development, Exp. Fluids **54**, 1469 (2013).
[62] R. Gupta and P. J. Ansell, Unsteady flow physics of airfoil dynamic stall, AIAA J. **57**, 165 (2019).
[63] R. B. Green, R. A. M. Galbraith, and A. Niven, The convection speed of the dynamic stall vortex, Technical Report TR920166, United States Air Force Office of Scientific Research, 1992.
[64] F. Malmir, G. Di Labbio, A. Le Floc'H, L. Dufresne, J. Weiss, and J. Vétel, Low-frequency unsteadiness in laminar separation bubbles, J. Fluid Mech. **999**, A99 (2024).
[65] C. Cura, A. Hanifi, A. V. Cavalieri, and J. Weiss, On the low-frequency dynamics of turbulent separation bubbles, J. Fluid Mech. **991**, A11 (2024).
[66] J. Jeong and F. Hussain, On the identification of a vortex, J. Fluid Mech. **285**, 69 (1995).

[67] C. E. Toppings and S. Yarusevych, Transient dynamics of stall and reattachment at low Reynolds number, J. Fluid Mech. **1011**, A38 (2025).
[68] M. S. H. Boutilier and S. Yarusevych, Separated shear layer transition over an airfoil at a low Reynolds number, Phys. Fluids **24**, 084105 (2012).
[69] B. J. Abu-Ghannam and R. Shaw, Natural transition of boundary layers—The effects of turbulence, pressure gradient, and flow history, J. Mech. Eng. Sci. **22**, 213 (1980).
[70] B. Thwaites, Approximate calculation of the laminar boundary layer, Aeronaut. Q. **1**, 245 (1949).
[71] M. Aniffa and A. C. Mandal, Experiments on the low-frequency oscillation of a separated shear layer, Phys. Rev. Fluids **8**, 023902 (2023).
[72] J. H. Almutairi, L. E. Jones, and N. D. Sandham, Intermittent bursting of a laminar separation bubble on an airfoil, AIAA J. **48**, 414 (2010).
[73] F. Crameri, Scientific colour maps (2018), https://www.fabiocrameri.ch/colourmaps/.
[74] F. Crameri, G. E. Shephard, and P. J. Heron, The misuse of colour in science communication Nat. Commun. **11**, 5444 (2020).